JRC Scientific and Technical Reports

Marine and Coastal Features of the Red Sea

Space and time heterogeneity of algal blooming, as seen by the Sea-viewing Wide Field-of-view Sensor (SeaWiFS), 1998-2006

Vittorio Barale

EUR 23091 EN - 2007

JRC EUROPEAN COMMISSION

Institute for Environment and Sustainability

The mission of the Institute for Environment and Sustainability is to provide scientific and technical support to the European Union's policies for protecting the environment and the EU Strategy for Sustainable Development.

European Commission
Joint Research Centre
Institute for Environment and Sustainability

Contact information
Address: V. Barale, TP 272, JRC EC, Via E. Fermi 2749, I-21027 Ispra (VA), Italy
E-mail: vittorio.barale@jrc.it
Tel.: +39 0332 789274
Fax: +39 0332 789034

http://www.ies.jrc.cec.eu.int
http://www.jrc.cec.eu.int

JRC 41911

EUR 23091 EN

ISSN 1018-5593

Luxembourg: Office for Official Publications of the European Communities

Printed in Italy

Title

Marine and Coastal Features of the Red Sea

Space and time heterogeneity of algal blooming, as seen by the Sea–viewing Wide Field–of–view Sensor (SeaWiFS), 1998–2006

Author

Dr Vittorio Barale
Institute for Environment and Sustainability
Joint Research Centre, European Commission
Via E. Fermi 2749 (tp 272), I-21027 Ispra (VA), Italy
Tel +39 0332 789274 Fax +39 0332 789034
e-mail: vittorio.barale@jrc.it

Abstract

Patterns of algal blooming, described by variations in the abundance of planktonic agents, are considered to be indicators of the ecological balance in coastal and marine environments. A time series of *chl* statistical maps and anomalies, derived from data collected by the Sea-viewing Wide Field-of-View Sensor (SeaWiFS), from January 1998 to December 2006, were considered to explore the space and time heterogeneity of algal blooming in the Red Sea. The imagery details the diverse characteristics of the northern (oligotrophic) sub-basin and the southern (mesotrophic) sub-basin, between which a central, transitional sub-basin presents more variable environmental conditions. The observed seasonal pattern is essentially bimodal, with a *fall-winter* period of extended blooming, followed by a *spring-summer* period of less intense blooming episodes, occurring in both the central sub-basin and the southern sub-basin. Overall, the annual bio-geo-chemical cycle seems to be governed by the climatic characteristics of the basin, the monsoon regime in particular, and by the ensuing thermohaline circulation. The *chl* interannual variability is not very pronounced, but there are hints of a steady *fall-winter* maxima increase, for most of the data set considered. The *chl* anomalies show limited oscillations around zero over the greater part of the basin. In the south, however, negative anomalies characterize the first half of the period considered, while positive anomalies prevail in the second half. A series of odd blooming episodes are also highlighted by both anomaly record and trend of the *chl* large-scale average.

Acknowledgements

The exploratory research described in the present report has been undertaken as part of the Framework Programme 7 (FP7) Action 21203 PROCAS. The images and data used in this report were acquired using the GES-DISC Interactive Online Visualization ANd aNalysis Infrastructure (Giovanni), provided by the NASA's Goddard Earth Sciences (GES) Data and Information Services Center (DISC).

Reference

V. Barale (2007). Marine and coastal features of the Red Sea. European Commission, EUR 23091 EN, pp. 56.

Table of Contents

Executive Summary

Patterns of algal blooming, described by variations in the abundance of planktonic agents, are considered to be indicators of the ecological balance in coastal and marine environments. Remote Sensing (RS) from Earth orbit can help assess these patterns over a range of space and time scales, monitoring at a glance the ecological dynamics of entire marginal and enclosed seas. In particular, optical RS allows basin-wide, multi-annual monitoring of chlorophyll-like pigments concentration (in the following referred to as *chl*).

A time series of *chl* statistical maps and anomalies, comprising nine consecutive full-year cycles, from January 1998 to December 2006, were considered to explore the space and time heterogeneity of algal blooming in the Red Sea. The data were derived from imagery collected by the Sea-viewing Wide Field-of-View Sensor (SeaWiFS), which started its mission in September 1997. The original top-of-the-atmosphere radiances were processed to correct atmospheric noise, to derive normalized water-leaving radiances and then to compute from these other derived parameters (*chl*). Single images were re-mapped on a common equal-area grid, and all valid pixels for a given time period and grid cell were averaged to compute monthly and yearly composites. Anomalies were derived by subtracting the climatological record from the composites.

The imagery details the diverse characteristics of the northern (oligotrophic) sub-basin and the southern (mesotrophic) sub-basin, between which a central, transitional sub-basin presents more variable environmental conditions. Hardly any subdivision between a strictly pelagic region and a costal zone appears anywhere in the Red Sea, with the exception of that occurring between the basin interior and the broad shelf areas, dotted by numerous islands, of the south.

The observed seasonal pattern is essentially bimodal, with a *fall-winter* period of extended blooming, which progresses from south to north, followed by a *spring-summer* period of less intense blooming episodes, occurring in both the central sub-basin and the southern sub-basin. Overall, the annual bio-geo-chemical cycle seems to be governed by the climatic characteristics of the basin, the monsoon regime in particular, and by the ensuing thermohaline circulation.

The *chl* interannual variability is not very pronounced, but there are hints of a steady *fall-winter* maxima increase, for most of the data set considered. The *chl* anomalies show limited oscillations around zero over the greater part of the basin. In the south, however, negative anomalies characterize the first half of the period considered, while positive anomalies prevail in the second half. A series of odd blooming episodes are also highlighted by both anomaly record and trend of the *chl* large-scale average.

1. Main Environmental Traits of the Red Sea

The Red Sea is a semi-enclosed tropical basin, bounded by north-eastern Africa, to the west, and the Arabian peninsula, to the east (International Hydrographic Organization, 1953). The elongated and narrow-shaped basin extends between the Mediterranean Sea, to the north-west, and the Indian Ocean, to the south-east (Plate 1). At the northern end, it separates into the Gulf of Aqaba and the Gulf of Suez, which is connected to the Mediterranean Sea *via* the Suez Canal. At the southern end, it is connected to the Gulf of Aden, and the outer Indian Ocean, *via* the Strait of Bal-el-Mandeb.

The Red Sea covers a wide span of latitudes, from 12°N to 30°N, and longitudes, from 32°E to 44°E (Plate 2). Within this geographical frame, the basin extends from north to south over a distance of approximately 1,900 km. Its average width from east to west is 280 km, with a maximum of 306 km, in the south, and a minimum of 26 km, in the Bab-el-Mandeb Strait. The two northern gulfs, Aqaba and Suez, are 180 km long and 25 km wide, and 300 km long and 50 km wide, respectively. The basin has a total area of about 440,000 km^2, a volume of 230,560 km^3, and more than 4,000 km of coastlines.

The formation of the Red Sea begun in the Eocene, when the African and Asian continental plates started to move apart (see lower left map of Plate 2 for details), and accelerated during the Oligocene. The basin acquired its present shape over the past 4 to 5 million years, by slow seafloor spreading, a fact that makes it a geologically recent opening and one of the youngest oceanic zones on Earth. Today, the basin continues to widen at a rate of 1-2 cm *per* year.

Due to the presence of wide, shallow continental shelves – about 25% of the basin is less than 50 m deep, 40% less than 100 m, and only 15% is more than 1000 m deep – the average depth of the basin is only 524 m. The shelf breaks are marked by extensive coral reefs, while the continental slope has an irregular profile, breaking into a series of steps down to about 500 m of depth. A central deep trench, sandwiched between the eastern and the western shelf, stretches from north to south for almost the entire axis of the basin. The deepest region lies between 14°N and 28°N and has a maximum depth of 2,920 m (3,040 m according to some sources). The deep areas are still geologically active and present numerous hydrothermal vents, emitting hot, salty and metal-rich brines. More than 20 Deeps have been discovered (*e.g.* the Atlantis II Deep, Discovery Deep, Oceanographer Deep), containing abundant metalliferous sediments and salt deposits[1]. The seafloor rises in the southern region toward the Bab-el-Mandeb Strait, just 137 m deep at the Hanish Sill. The two

[1] Sometime during the Paleogene (Tertiary) period, the Bab-el-Mandeb is thought to have closed – either because of volcanic eruptions at Perim Island or due to sea level lowering during the Ice Ages) – causing the early Red Sea to evaporate, and creating the salt beds.

gulfs in the northern region are similar in shape, but their bottom topography is not. The Gulf of Suez is shallower and has a relatively flat bottom, with depths ranging from 55 to 73 m. The Gulf of Aqaba, instead, comprises a deep basin – separated by a submarine sill into two pits, both deeper than 1,000 m – bordered by a narrow shelf.

The Red Sea is surrounded by desert or semi-desert areas, with no major freshwater inflow. Given the absence of rivers and permanent streams, occasional runoff is due only to seasonal torrents (wadis). In this arid region, the weather is characterized by extremely high temperatures, particularly in summer, increasing from the northern to the southern area (which is considered to be among the hottest in the world). Air temperatures range from 6 to 39 °C at the Suez Canal and from 13 to 42 °C along the coast of the Arabian peninsula. Rainfall is extremely sparse and occurs usually in the form of short, local showers, often associated with thunderstorms and occasionally with dust storms. The annual rainfall over the Red Sea region is extremely low, averaging about 110 mm *per* year (but only half of that, about 60 cm *per* year, for the Red Sea itself and its coastal zones).

The climate of the Red Sea is characterized by two distinct seasons, under the influence of the north-east monsoon (winter) and the south-west monsoon (summer), respectively (Morcos, 1970). Monsoon winds occur because of the differential heating between landmasses and ocean surface. These geographic and climatic conditions, leading to a low freshwater input, due to either continental runoff or precipitation, and a high evaporation rate, make the Red Sea one of the hottest and saltiest bodies of seawater in the world.

The average surface temperature in summer ranges from 26 °C in the north to 30 °C in the south, with variations of only 2 °C in winter. In general, surface temperature declines toward Bab-el-Mandeb, due to exchanges with the Gulf of Aden, and gradually decreases toward the northern region. Deeper waters are stable throughout the region, so that below 300 m the temperature is constantly between 21 and 22 °C. Salinity is also high, due to the combination of high evaporation, low precipitation and lack of river outflow. It ranges between 36 and 39 psu, and is usually lower in the southern region, again due to the exchanges with the Gulf of Aden. Water renewal in the Red Sea is relatively slow, as the exchange with the outer ocean takes approximately 6 years for the 200 m layer above the thermocline, but approximately 200 years for the entire sea.

The Red Sea circulation follows an anti-estuarine pattern, with relatively fresher water entering the basin above an outflowing saltier, denser layer (Bower *et al.*, 2002). The fresher Gulf of Aden Surface Water (GASW) enters the Red Sea via the Bab-el-Mandeb. Within the basin, the GASW is subject to the aforementioned excess of evaporation over precipitation and runoff, estimated to be 2.06 ± 0.22

m yr^{-1} (Sofianos *et al.*, 2002). This net evaporation drives the formation of Red Sea Water (RSW) in the northern part of the basin (Eschel *et al.*, 1994). This northern RSW flows southwards as a dense, cool, salty layer, under which resides a relatively stagnant layer of still denser Red Sea Deep Water (RSDW), formed during the winter months in the Gulf of Suez and Gulf of Aqaba (Eschel *et al.*, 1994). The Red Sea thermohaline circulation is modified in the upper two layers (GASW and RSW) by the action of the wind field and rotation, which help generate a system of gyres, eddies and boundary currents (Quadfasel and Baudner, 1993).

In the Red Sea, detailed current data are lacking, partially because currents are weak and variable, both spatially and temporally (Siedler, 1969). Such space and time variations are essentially wind-driven. In summer, the prevailing winds drive surface waters south, whereas in winter the mean flow is reversed. Over the full annual cycle, the net value of the latter predominates, resulting in an overall drift to the northern end of the Red Sea, where evaporation generates the RSW, which then moves southward, and ultimately leave the basin at intermediate depth (Grassen and Kroon, 1991).

Unlike that of many other marginal seas, the Red Sea overflow is strongly seasonal, due to the monsoon winds and to variations in buoyancy fluxes, with a winter maximum of 0.6 Sv and a summer minimum of 0.05 Sv [2] (Murray and Jones, 1997). In the colder months (November to May), a two-layer system dominates the exchange over the Hanish Sill: GASW enters the Red Sea above the RSW layer (while the underlying RSDW leaves the basin at a much slower rate, via a combination of mixing into the RSW above it and of Bernoulli aspiration, without significantly altering the two-layer exchange; Smeed 1997). In the warmer months (June to October), the Gulf of Aden Intermediate Water (GAIW), present under the GASW, is upwelled in the Gulf of Aden by the south-west monsoon winds. As the GAIW upper interface rises, it penetrates into the southern Red Sea as an intermediate layer. The intrusion can last for a period of 3 months and is mixed into the upper layer, inducing an occasional GASW flow reversal (Smeed, 2000).

Tides are small in the Red Sea, ranging from 0.6 m in the north, near the mouth of the Gulf of Suez, to 0.9 m in the south, near the Gulf of Aden, but fluctuating between 0.2 and 0.3 m away from the nodal point. The Central Basin is therefore almost tideless, and thus annual water level changes appear to be more significant than tides. In spite of the small tidal range, extensive near-coastal areas and lagoons can be inundated by a thin sheet of water during high tide, especially along the coast of the Arabian peninsula.

[2] The Sverdrup is a unit of measure for large oceanic flows: 1 Sv = 10^6 m^3 s^{-1}.

The Red Sea has low productivity, due to a strong nutrient limitation, given the absence of major continental inflows and the presence of a permanent thermocline, which inhibits benthic nutrients from mixing into surface waters where most primary production occurs (Edwards, 1987). The main nutrient input is from the Indian Ocean, through the Gulf of Aden and the southern part of the Red sea (Sheppard *et al.*, 1992). In spite of these general conditions, the Red Sea constitutes a rich and diverse ecosystem. More than 1100 species of fish have been recorded, with about 10% of these being endemic. This rich diversity is in part due to the 2000 km of coral reefs, and other particular habitats, such as mangrove forests, seagrass beds, salt marshes and salt pans, distributed throughout the region (Sheppard, 2000).

These unique habitats support a wide range of marine life, including sea turtles, dugongs, dolphins and many endemic fish species. Coral reefs mainly extend along the northern and central coasts, and decrease in abundance towards the southern region, as coastal waters become more turbid. In the central region, corals are mainly found 3-10 km offshore, along a narrow bank, forming a large barrier reef structure that runs parallel to the coastline. The most extensive areas of coral reefs are found along the Arabian peninsula coast, with over 194 recorded species. Mangrove forests are scattered along much of the coastline, but their highest concentration is in the southern region, due to the soft bottom substrate. Various species of seagrass are widespread in the basin, and are most common in the lagoons and embayments of the southern region.

Seven countries border the Red Sea[3], namely Egypt, Sudan, Eritrea, Yemen, Saudi Arabia, Jordan and Israel. However, the region is sparsely populated, and no more than 5 million people are estimated to live along the coast. The area of Jeddah, in Saudia Arabia, with over 2 million residents, has the highest population. The major industries in the region are linked to oil exploration, extraction, processing and transport. In fact, in spite of the fame due to its natural beauty, the Red Sea constitutes a major shipping route for oil tankers and other vessels travelling through the Suez Canal. Fisheries and, more recently, tourism also started to play an important role in the local economy. Though the Red Sea accounts for 0.123% of the total world ocean area, its contribution to the world fish catch is only 0.07% (Head, 1987). Nevertheless, it has fish resources – including classical fisheries, but also fish collection for aquarium trade, as well as pearl oyster and shrimp farming – that are significant to the countries in the region, providing a good source of protein and livelihood for coastal communities (Tesfamichael and Pitcher, 2006). Due to the high diversity of marine life and favourable climate, tourism has also

[3] CIA (2004). World Factbook. http://www.odci.gov/cia/publications/factbook/

become a major factor in many Red Sea countries, with over 1 million tourists per year expected in the future.

Although the Red Sea has remained relatively free of pollution, its environment is currently under increasing threat from a wide range of human activities, both land-based and, primarily, marine-based (Gladstone *et al.*, 1999). Destruction of habitat, due to urban expansion, industrial development and tourism, is growing. So is the over-exploitation of some living marine resources, such as lobsters, sharks and sea turtles. The Red Sea has several marine protected areas, the best known being the Ras Mohammed National Park, at the southern tip of the Sinai Peninsula; Hurghada and the adjacent islands along the Egyptian coast; Sanganeb atoll in Sudan; and the Farasan Islands in Saudi Arabia.

A regional Convention for the Conservation of the Red Sea and Gulf of Aden Environment, also known as the Jeddah Convention, was signed in 1982 by all riparian countries. This international agreement is somewhat focused on addressing pollution problems, and provides the main legal framework for cooperation on marine issues in the region. An official intergovernmental organization, known as the Regional Organization for the Conservation of the Red Sea and Gulf of Aden (PERSGA) was established in 1995, as an implementation body of the Jeddah Convention, dedicated to the conservation of the coastal and marine environment. A Strategic Action Plan (SAP) for the Red Sea and Gulf of Aden has been prepared by PERSGA, and implemented as a major new international initiative in 1998 (PERSGA, 1998).

Plate 1. Red Sea, simulated true-colour from MODIS data, 30.08.2004

Plate 2. Red Sea Geographical Map and Bathymetry

2. The Red Sea in the SeaWiFS (1998-2006) Historical Record

Patterns of algal blooming, described by variations in the abundance of planktonic agents, are commonly adopted as indicators of ecological balance in coastal and marine environments. Remote Sensing (RS) from Earth orbit can help assess these patterns over a range of space and time scales, monitoring ecosystem dynamics of entire marginal or enclosed seas (Barale, 1994). Optical RS, in particular, allows large-scale, long-term monitoring of chlorophyll-like pigments concentration (in the following referred to as *chl*). Following analogous studies of the Mediterranean Sea and Black Sea (Barale *et al.*, 2004; Barale *et al.*, 2005; Barale and Jaquet, 2006), the present report uses an extended time series of *chl* statistical maps and anomalies to explore the space and time heterogeneity of algal blooming in the Red Sea.

The data set used here was generated by the Sea-viewing Wide Field-of-View Sensor (SeaWiFS). The SeaWiFS mission, which started in September 1997, has generated an extensive collection of world-wide optical RS data (McClain *et al.*, 2004). Nine consecutive full-year cycles, from January 1998 to December 2006, were considered to follow *chl* dynamics in the Red Sea. The data being presented should be considered with caution, owing to the presence of coloured water constituents, or to direct bottom reflection, which may significantly alter the *chl* signal derived from the sensor measurements, particularly in shallow coastal areas. In fact, the presence of optically active materials other than phytoplankton and related pigments (*i.e.* dissolved organic matter and suspended inorganic particles), with partially overlapping spectral signatures, can prevent the computation of reliable *chl* absolute values. However, when the limitations above are accounted for, the analysis of historical times of satellite data can provide at least qualitative information on recurrent or anomalous algal blooms, and related environmental boundary conditions.

2.1 The *chl* Data Set for the Red Sea

The data set considered here to assess the evolution of the *chl* field in the Red Sea is that collected by the SeaWiFS from 1998 to 2006. Composite and climatological data were obtained directly from the National Aeronautics and Space Administration (NASA). The original imagery was processed[4] to correct top-of-the-atmosphere radiances from atmospheric noise, to derive normalized water-leaving radiances L_{WN} and then to compute from these all other derived parameters (including *chl*). Each daily image was treated using the SeaDAS algorithm set (Baith *et al.*, 2001) and re-mapped on a common equal-area grid, with a grid cell, or "bin", of 9 km x 9 km. For the creation of the monthly and yearly data products, all of the valid pixels for a given time period and grid cell were compiled in the same bin, and their

[4] SeaWiFS Ocean Reprocessing 5.1 completed on July 5, 2005. For details see the www site: http://oceancolor.gsfc.nasa.gov/REPROCESSING/SeaWiFS/R5.1/

weighted mean generated. The weight was based on the number of valid pixels used in the binning process (Campbell *et al.*, 1995).

Single images at full resolution (~1.2 km at nadir) can show a significant amount of detail in the patterns traced by *chl*. However, they may be incomplete, over a given area, because of imaging geometry, algorithm failure or cloud cover. Hence the choice of using composite images, to assess the main characteristics of surface waters from a statistical point of view. Because the number of valid pixels increases with larger and longer binning intervals, the compositing process generates complete, cloud-free images. As will be seen in the following, though, the variability due to highly dynamical events in a given area is averaged out too, and the composite images retain only those patterns that persist over significant areas and periods of time.

In order to characterize transient and recurrent variability, at the various space/time scales considered, the composite images were compared with the climatological record to derive *chl* anomalies. The available monthly and yearly climatologies are defined as averages of all composite images in each time period, over the entire SeaWiFS lifetime (*i.e.* from September 1997 to September 2007, at the time when the present work was carried out). The *chl* anomalies, again at the monthly and yearly scales, are defined as the difference between each monthly mean and the corresponding climatological month, and between each yearly mean and the climatological year, respectively.

2.2 The *chl* Reference Climatology for the Red Sea

The Red Sea climatological yearly mean (Plate 3), derived from the SeaWiFS 1998-2006 data set, shows a *chl* field differentiated between successive latitudinal zones. The two Gulfs at the northernmost latitudes (28-30°N) appear to be quite different from one another, with the Gulf of Suez presenting mean concentration a factor 2 higher than that of the Gulf of Aqaba (*i.e.* 0.4 *vs* 0.2 mg m^{-3}). The area immediately to the south, which in the following will be referred to as the "Northern Basin" (22-28°N), has a decisively oligotrophic character, with a mean concentration on the order of 0.2 mg m^{-3}. Further south, the area that in the following will be referred to as the "Central Basin" (18-22°N) presents higher concentrations, from 0.4 to 0.6 mg m^{-3} in the near-coastal zones, and up to 1.0 mg m^{-3}, or more, right along the coastlines. Finally, at the southernmost latitudes, in the area that in the following will be referred to as the "Southern Basin" (12-18°N), wide near-coastal bands display concentrations >1.0 mg m^{-3}, in particular around the Dahlak Archipelago and the Farasan Islands, while lower concentrations, ranging from 0.6 to 1.0 mg m^{-3}, appear in the central part of this sub-basin, north of the Hanish Islands.

As noted above, the range of SeaWiFS-derived *chl* values should be considered in a relative sense. Standard bio-optical algorithms – based

on the inverse dependence between *chl* and the ratio between normalized water-leaving radiances in the blue and green spectral intervals – such as those used to generate the present SeaWiFS data products, have been shown to perform significantly worse at regional rather than global scales (Gregg and Casey, 2004). Keeping in mind this potential (but systematic) uncertainty, the historical data seem to indicate that the background characteristics of the Red Sea *chl* field are closely coupled to the geographic and climatic setting of the basin.

The climatological monthly means (Plate 4) show a more structured *chl* field, which presents a certain degree of variability in all of the sub-basins identified in the yearly mean. Algal blooming is apparent everywhere (except that in the interior of the northern basin, where *chl* values never exceed 0.2 mg m^{-3}) already in January and reaches a relative maximum in February, only to decline somewhat in March. Then, in April, May and June, the blooming continues to decrease in both size and intensity, in particular in the Southern Basin. In July, August and September, a *chl* minimum is reached over the entire Red Sea[5], while the interior of the Northern Basin exhibits the lowest *chl* values of the entire seasonal sequence. This absolute minimum is followed by a renewal of the blooming in October, November and December, starting from the Southern Basin and progressing northward, towards the same conditions already seen in January.

A more schematic way of looking at the phytoplankton seasonal cycle in the Red Sea is proposed in Plate 5, where the *chl* average basin value (ABV), derived from the climatological monthly means, is plotted against time. In this case, which includes all pixels in the area 12-28°N and 34-44°E of each climatological month in the computation of the *chl* AVB (see map in the lower left section of Plate 5), a maximum is reached from October to March, while the minimum occurring from March to October is interrupted by relative maxima in June and August. Although this trend recalls the one inferred from the above analysis of the climatological monthly mean images, it appears to be critically dominated by the anomalous summer values of the Southern Basin, where persistent cloud cover alters the area over which the *chl* ABV is computed, favouring the impact of high near-coastal values.

Considering only the Northern Basin (see map in the lower right section of Plate 5), the *chl* average presents just a slight increase in winter, with maximum in February (Plate 6, upper panel). By contrast, considering only the Central Basin (map in Plate 5), a rather different seasonality emerges, with two maxima, in winter, from December to January, and in summer, from June to July (Plate 6, middle panel). Likewise, in the Southern Basin (map in Plate 5), two analogous maxima occur in November and in July (Plate 6, lower panel).

[5] Note that persistent overcast conditions prevented (for 9 consecutive years!) the imaging of most of the Southern Basin in July, hampering somewhat the following statistical analyses.

Plate 3. SeaWiFS-derived chl Climatological Annual Mean

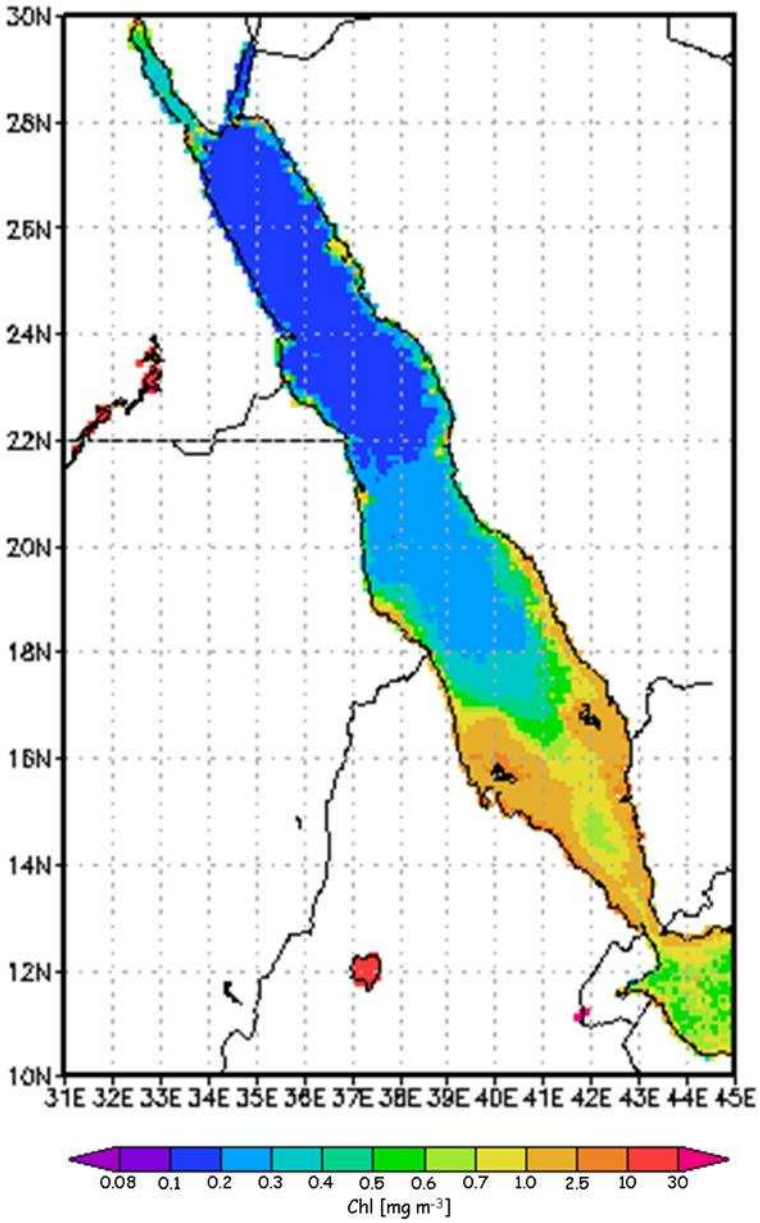

Plate 4. SeaWiFS-derived chl Climatological Monthly Means

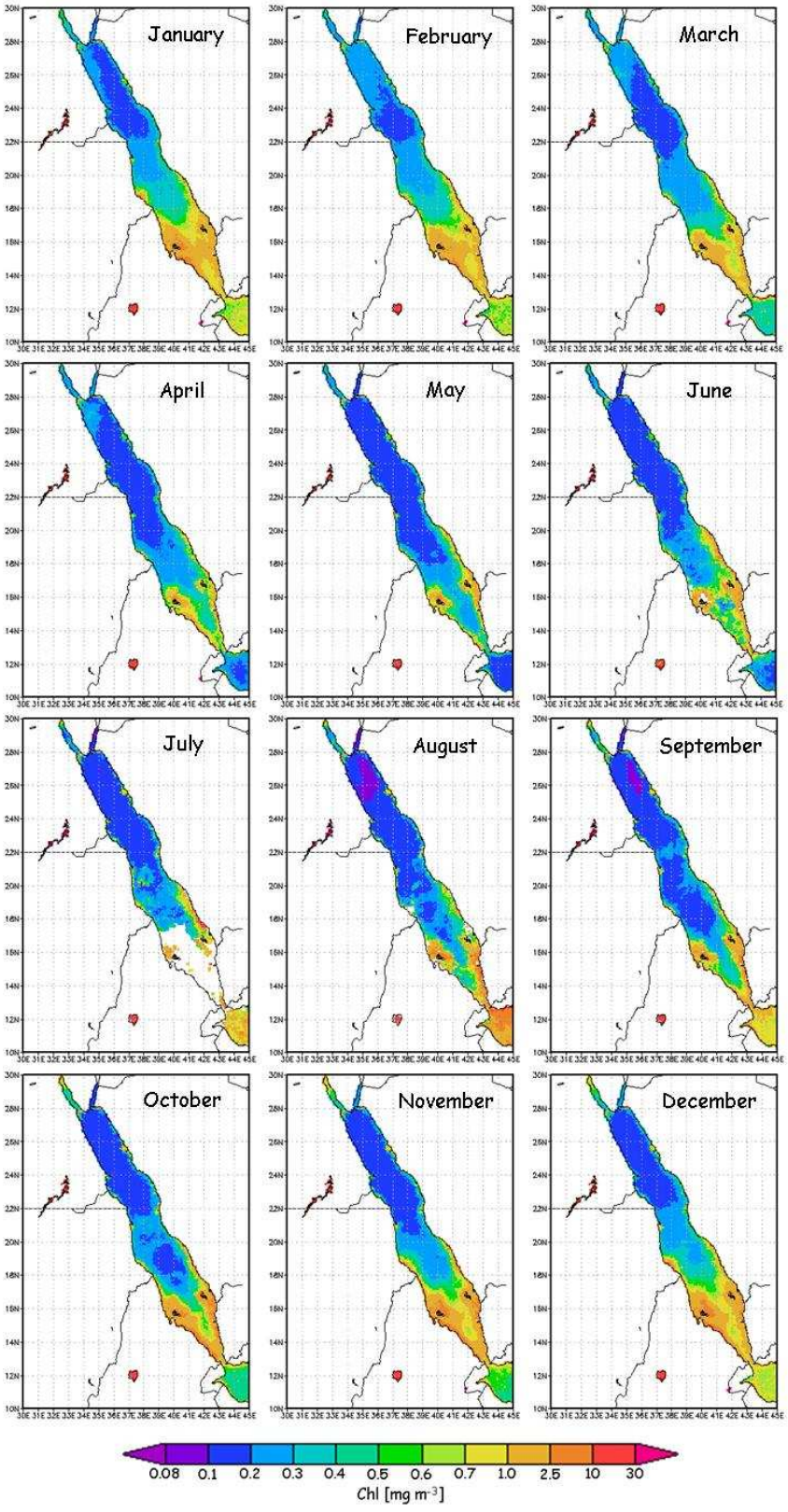

*Plate 5. Trend * of the chl Climatological Monthly Means, ABV ***

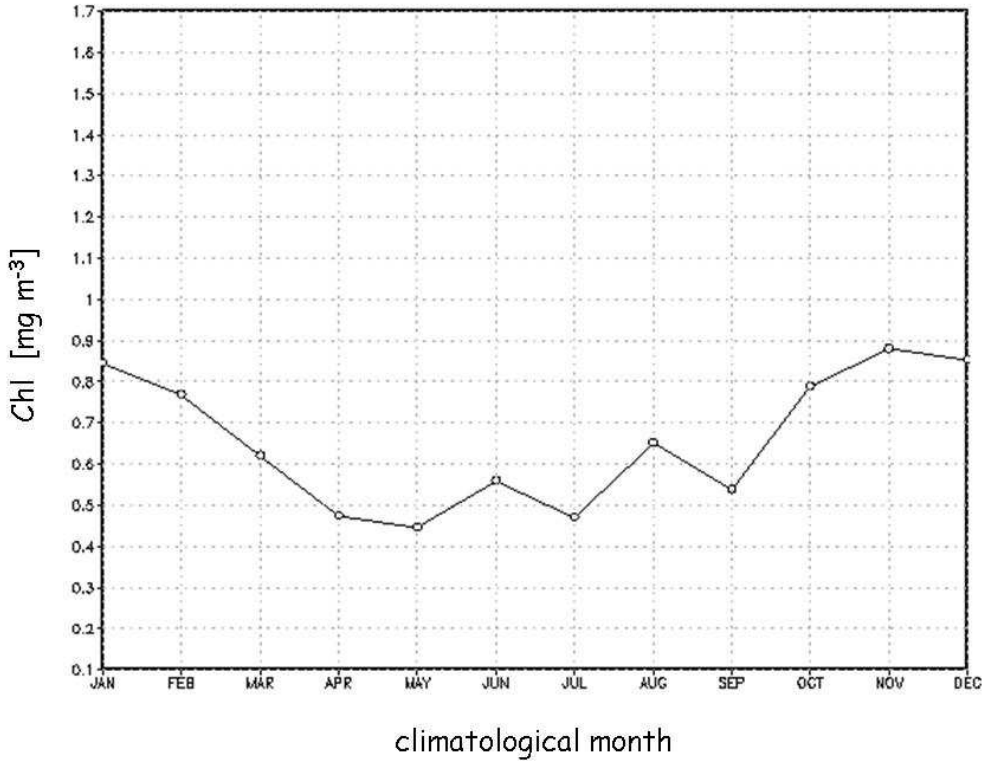

* Y axis: *chl* average basin value [mg m^{-3}], min 0.1, max 1.7, interval 0.1
X axis: climatological months (January to December)

** The Average Basin Value (ABV) is computed over the Red Sea area 12-28 N, 34-44 E; other regions considered to compute the *chl* climatological monthly mean trend are:
- the Northern Basin (22-28 N, 34-38 E),
- the Central Basin (18-22 N, 37-41 E),
- the Southern Basin (12-18 N, 38-44 E),
according to the following map subsets (shown on the *chl* climatological annual mean) :

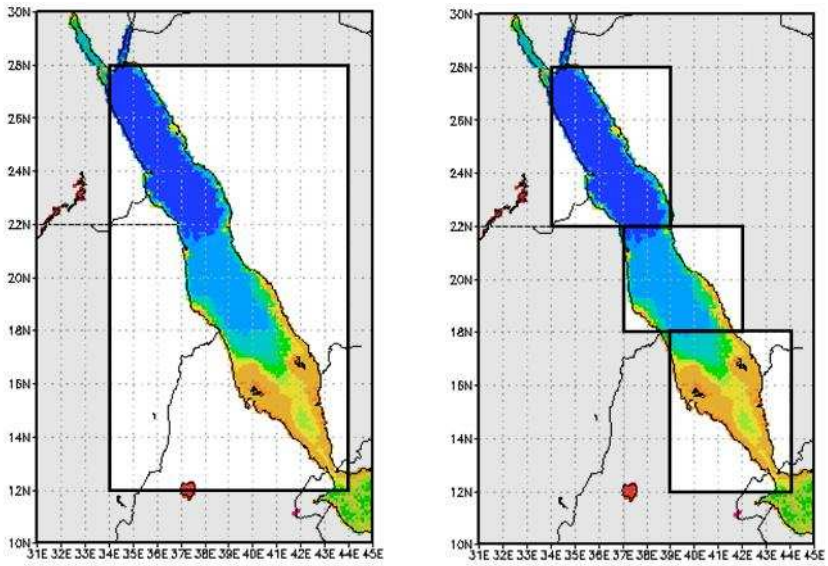

*Plate 6. Trend * of the chl Climatological Monthly Means, sub-regions***

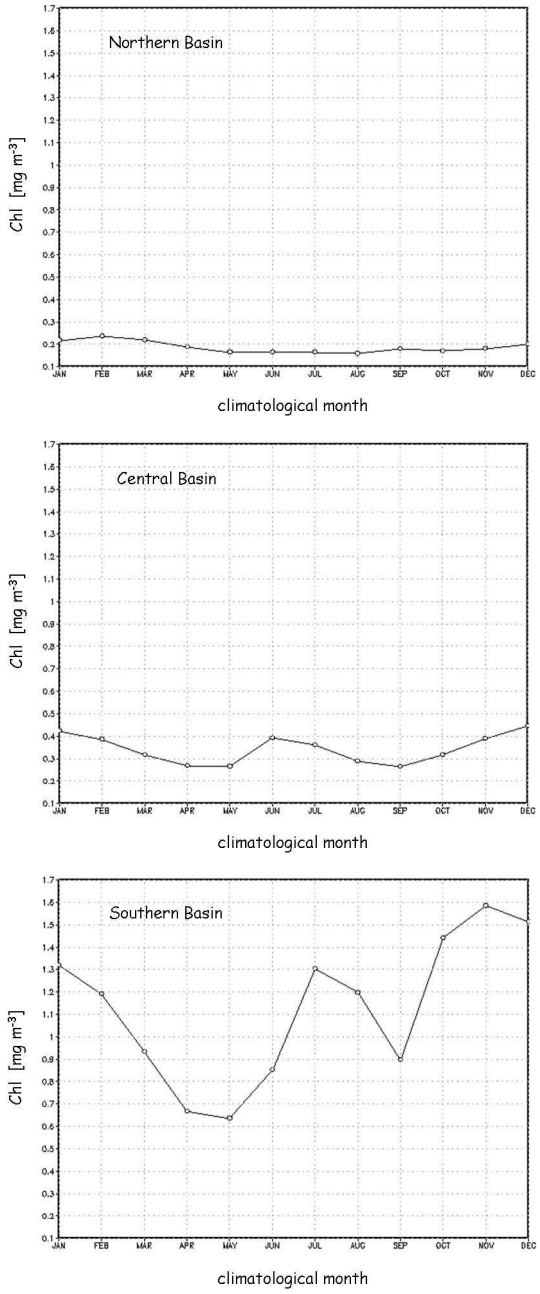

* Y axis: *chl* average basin value [mg m^{-3}], min 0.1, max 1.7, interval 0.1
X axis: climatological months (January to December)

** upper panel: Northern Basin (22-28 N, 34-38 E)
middle panel: Central Basin (18-22 N, 37-41 E)
lower panel: Southern Basin (12-18 N, 38-44 E)

3. Interannual and seasonal variability of *chl* in the Red Sea

The *chl* yearly means, shown in Plate 7, exhibit space patterns rather similar to those appearing in the climatological images. While the Northern Basin maintains its characteristics throughout the data set, its oligotrophic character seems to extend also into the Central Basin in several instances (1999, 2000, 2001 and again 2003, 2004, 2005). The features of the Southern Basin, instead, appear to be quite constant, and to be anchored rather closely to the main bathymetric relief of the near-coastal zone (in particular over the shallow banks around the Dahlak Archipelago, the Farasan Islands, the Hanish Islands and in the Bab-el-Mandeb). Only the lower *chl* values near the central part of this sub-basin display a broad interannual variability, ranging from 0.5-0.6 mg m^{-3} (as *e.g.* in 1998 and 2000) to 0.7-1.0 mg m^{-3} (as *e.g.* in 2004 and 2006).

The *chl* yearly anomaly maps, shown in Plate 8, highlight geographical spread and absolute value of the Red Sea blooming patterns that differ, in each yearly mean, from the corresponding climatological mean. The series shows that most anomalies pertain to the Southern Basin (mainly negative anomalies in the first half of the period covered by the data set, and mainly positive anomalies in the second half). In the Central Basin, sizeable anomalies occurred only in 1998 and, to a lesser extent, in 2002. Virtually no significant anomalies appear in the Northern Basin, except for a feeble signal at the northernmost part of the sub-basin in 2000.

The upper section of Plate 9 shows the series of *chl* ABV, computed for each of the 12 monthly means and for the 9 years considered, and plotted against time. The general trend appearing in this case, where the ABV includes all pixels in the area 12-28°N and 34-44°E for each monthly mean (see map in the lower left section of Plate 9), suggests a steady increase of the range between lower summer minima and, in particular, higher winter maxima. This trend is not maintained in every sub-basin, when the *chl* average is computed using only values from the Northern Basin (Plate 10, upper panel), the Central Basin (Plate 10, middle panel), and the Southern Basin (Plate 10, lower panel), as was done already for the climatological monthly means (see map in the lower left section of Plate 9).

In the sub-basin plots of Plate 10, the Northern Basin shows hardly any interannual variability, while the Central Basin is characterized by an irregular pattern, possibly contaminated by noise due to the cloud cover of summer months. The same noise can also be seen in the Southern Basin (note that summer data are missing completely in 2000, 2003 and 2006), where however somewhat higher values recur in the latter part of the data set (as already seen also in the Central Basin). The incidence of missing data generated by persistent overcast

conditions, at the monthly scale, can be readily evaluated from the sequence of monthly mean images shown in Plate 11.

In a schematic way, two main periods, split again into two distinct phases, seem to emerge from the data set presented in Plate 11. The first period, which will be referred to as "*fall-winter*", but that goes roughly from October to March, is characterized by clear skies, and by higher *chl* values. The second period, which will be referred to as "*spring-summer*", but that goes roughly from April to September, is characterized by persistent cloud cover, and by lower *chl* values.

In *fall-winter*, the first 3-month phase, from October to December, shows increasing *chl* values almost everywhere. Starting from the relative minimum of October, a maximum is reached already in November, in the Southern Basin, and then in December, elsewhere. The second 3-month phase, from January to March, shows decreasing *chl* values almost everywhere. Thus, starting from the maximum of January, or February in the Northern Basin, a relative minimum for the period is reached again in March.

In *spring-summer*, the first 3-month phase, from April to June, shows the *chl* values continuing their decline and reaching an absolute minimum around May. Then the mean values start to grow again in June, as observed in the Central Basin and particularly in the Southern Basin. In the second 3-month phase, from July to September, the increase seems to continue, until a relative maximum is reached in July or August (even if any trend observed in this phase must be considered with caution, due to the persistent, sometimes total, cloud cover), while another relative minimum follows in September.

The overview of *chl* monthly means (Plate 11) illustrates a substantial seasonal variability, but not a significant interannual variability (except for a score of anomalous features that will be detailed in the following). The 1998 series (Plate 12) presents the same patterns described for the climatological means, but with a large summer anomaly appearing in the Central basin. This anomaly appears also as a spike (the largest in the whole data set) in the corresponding plot of Plate 10. A similar general pattern is repeated in the 1999 series (Plate 13) and in the 2000 series (Plate 14), although without any summer anomaly. In 1999, the presence of a strong eddy field in the Northern Basin is suggested by the February mean, while in 2000 this area presents a lasting bloom, developing in February and continuing in March and April, south of the Jamsah Promontory.

The same northern bloom reappears anew, on a somewhat reduced scale, in February and March of 2001 (Plate 15), and then again in February 2002 (Plate 16). In the second half of 2002, a large eddy seems to develop between the Southern Basin and the Central Basin,

where strong anomalous blooming appears in October and, to a lesser extent, in November. Again this bloom corresponds to a sizeable spike in the matching plot of Plate 10. Then, in 2003 (Plate 17), the *chl* field returns once more to the usual pattern of higher values in winter and lower values in summer, over most of the Red Sea.

The standard climatological sequence continues to reappear in 2004 (Plate 18), 2005 (Plate 19) and 2006 (Plate 20). However, longer overcast conditions seem to characterize the summers of this last part of the data set, with extensive persistent cloud cover starting already in June, in the Central Basin and primarily in the Southern Basin, and continuing until September. Hence, the noisier data set of this period, resulting from the restriction of the *chl* ABV computation to a smaller number of pixels, could be responsible, at least in part, for the trend observed in the plots of Plates 9 and 10 (but not for the late 2005 and early 2006 spike appearing in the plots of Plate 10, which in fact is due to unusual blooms, in the Central Basin particularly) .

The upper section of Plate 21 shows a plot against time of the *chl* anomaly ABV, computed over all pixels in the area 12-28°N and 34-44°E (see usual map in the lower left section of Plate 21) for each of the 12 monthly means and for the 9 years of the data set. As for the *chl* averages, the general trend is again that of a slight increase of the anomalies in the latter part of the period considered. And, again, the trend is not maintained in every sub-basin, when the *chl* average is computed using only values from the Northern Basin (Plate 22, upper panel), the Central Basin (Plate 22, middle panel), and the Southern Basin (Plate 22, lower panel), according to the maps shown in the lower left section of Plate 21. The anomalies are essentially zero in the Northern Basin, and very small in the Central Basin, except for the three notable spikes of July 1998, October 2002 and January 2006. Conversely, in the Southern Basin, much larger anomalies appear in the second half of the period considered, even thought the extremely noisy appearance points once more to an abnormally high variability due to the variable and widespread cloud coverage of this sub-basin.

Plate 7. SeaWiFS-derived chl Yearly Means

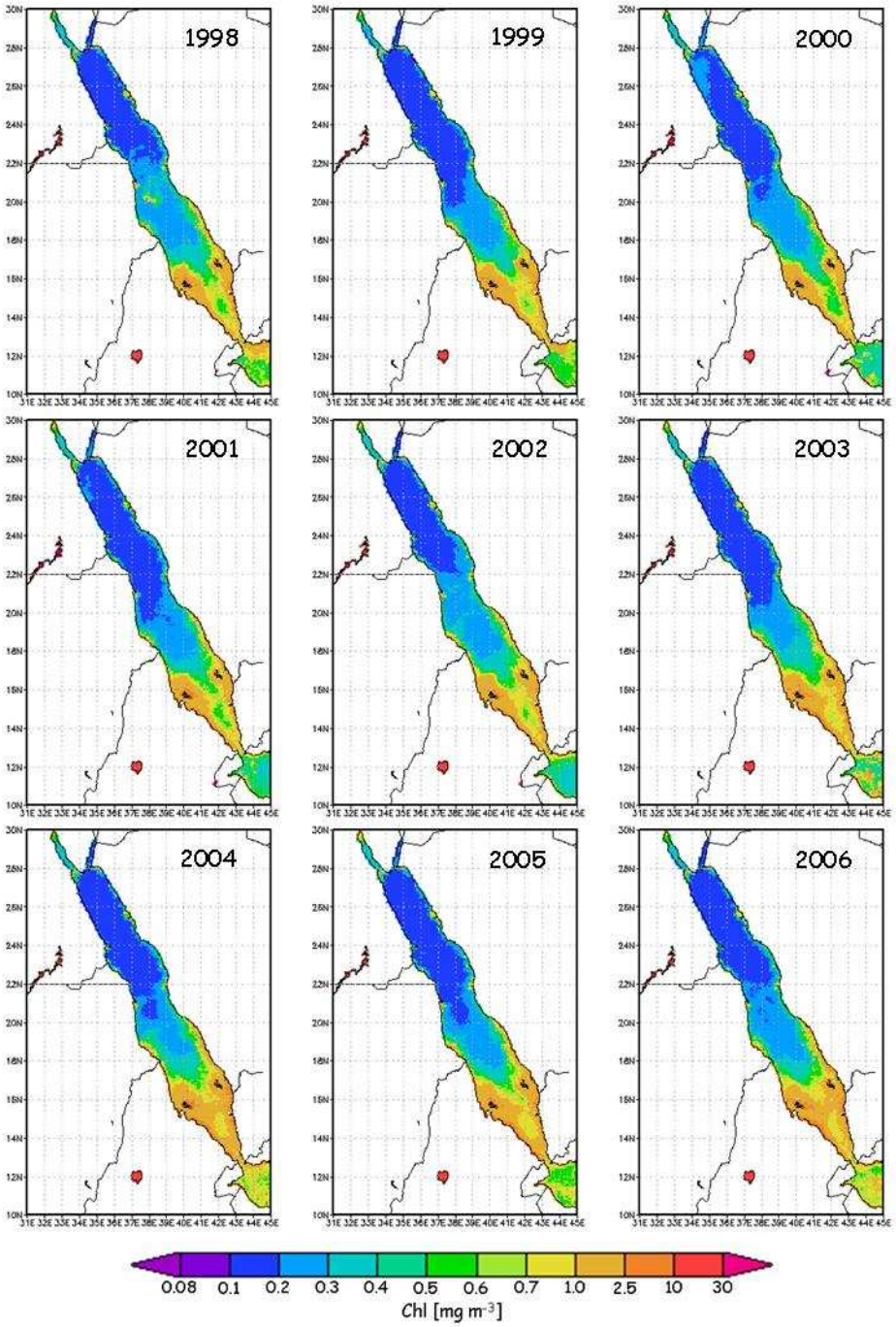

Plate 8. SeaWiFS-derived chl Yearly Anomalies

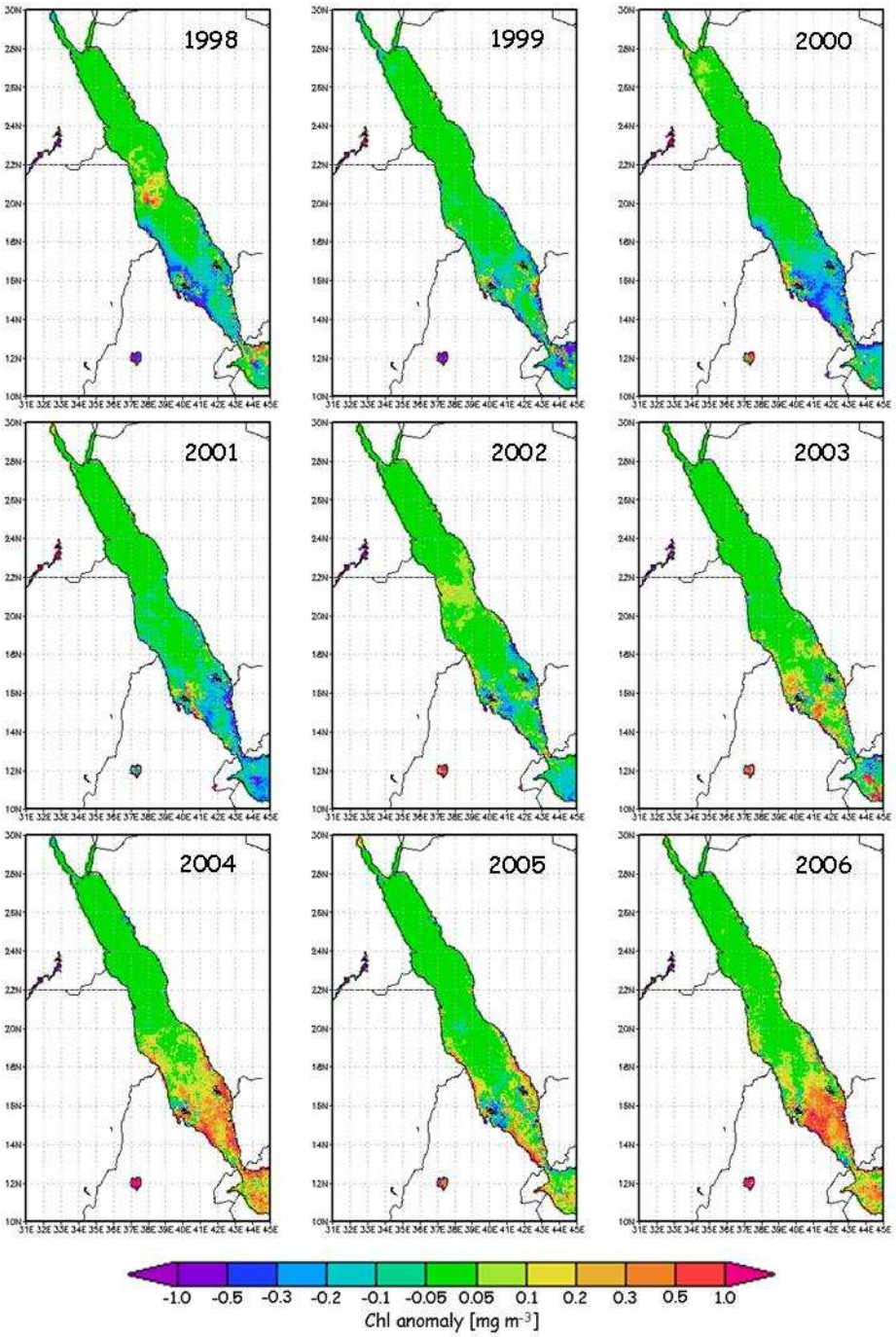

*Plate 9. Trend * (interannual) of the chl Monthly Means, ABV ***

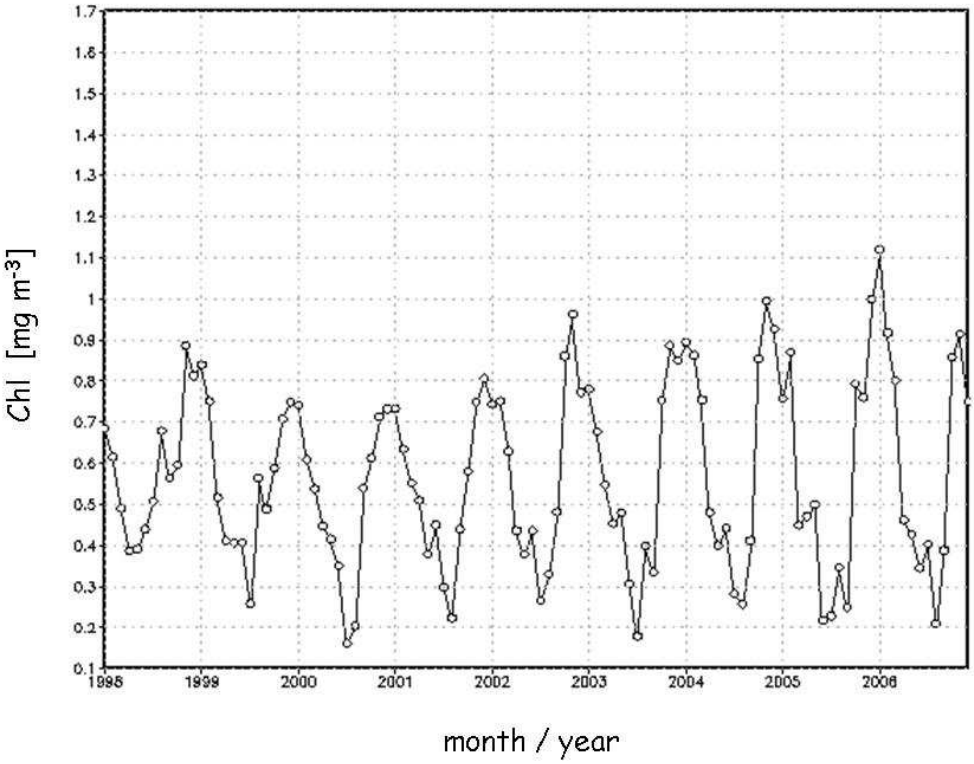

* Y axis: *chl* average basin value [mg m^{-3}], min 0.1, max 1.7, interval 0.1
X axis: months (January to December) and years (1998 to 2006)

** The Average Basin Value (ABV) is computed over the Red Sea area 12-28 N, 34-44 E; other regions considered to compute the *chl* climatological monthly mean trend are:
- the Northern Basin (22-28 N, 34-38 E),
- the Central Basin (18-22 N, 37-41 E),
- the Southern Basin (12-18 N, 38-44 E),

according to the following map subsets (shown on the *chl* climatological annual mean) :

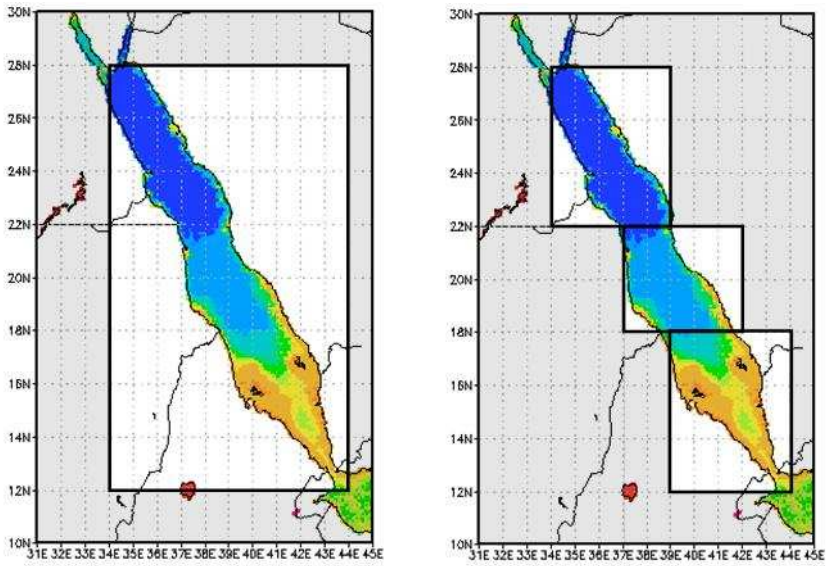

*Plate 10. Trend * of the chl Climatological Monthly Means, sub-regions***

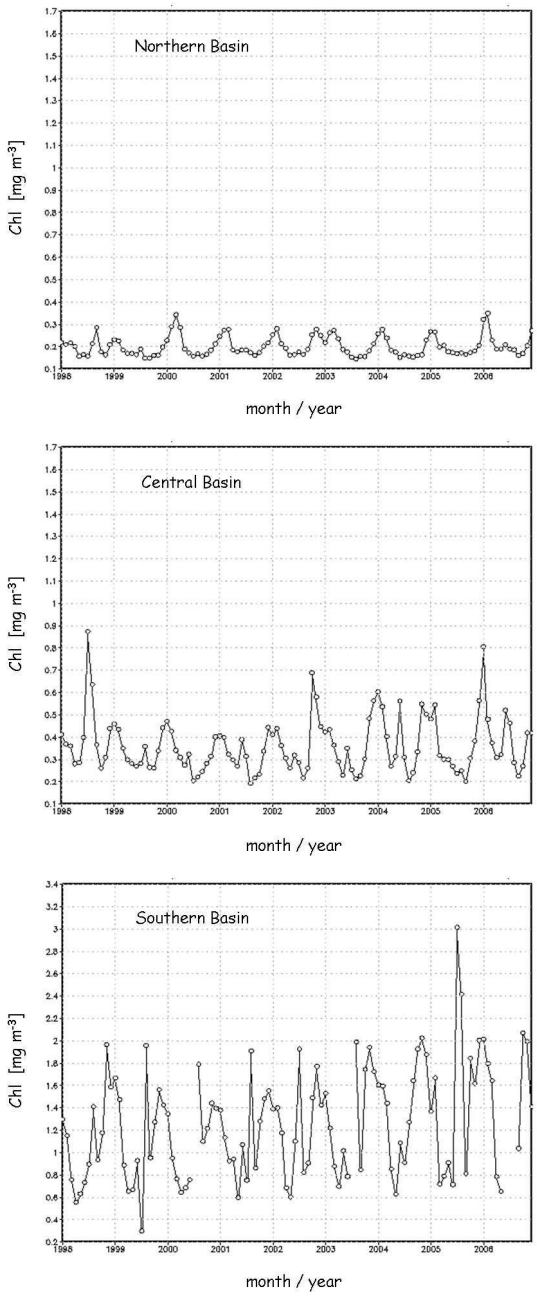

* Y axis: *chl* average basin value [mg m^{-3}], min 0.1, max 1.7, interval 0.1
(but for the Southern Basin: min 0.2, max 3.4, interval 0.2)
X axis: months (January to December) and years (1998 to 2006)

** upper panel: Northern Basin (22-28 N, 34-38 E)
middle panel: Central Basin (18-22 N, 37-41 E)
lower panel: Southern Basin (12-18 N, 38-44 E)

Plate 11. SeaWiFS-derived chl Monthly Means: 1998 to 2006

Plate 12. SeaWiFS-derived chl Monthly Means: 1998

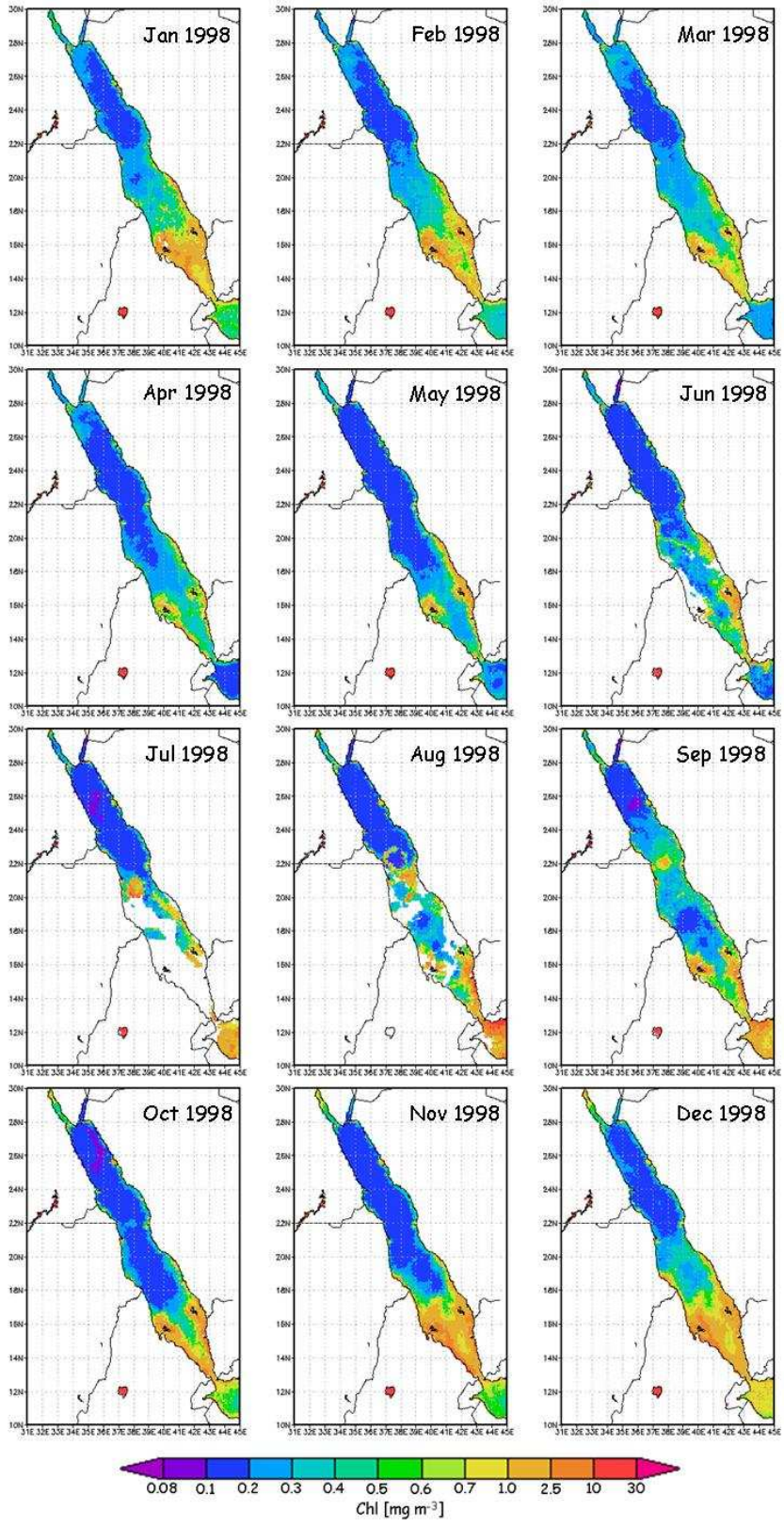

Plate 13. SeaWiFS-derived chl Monthly Means: 1999

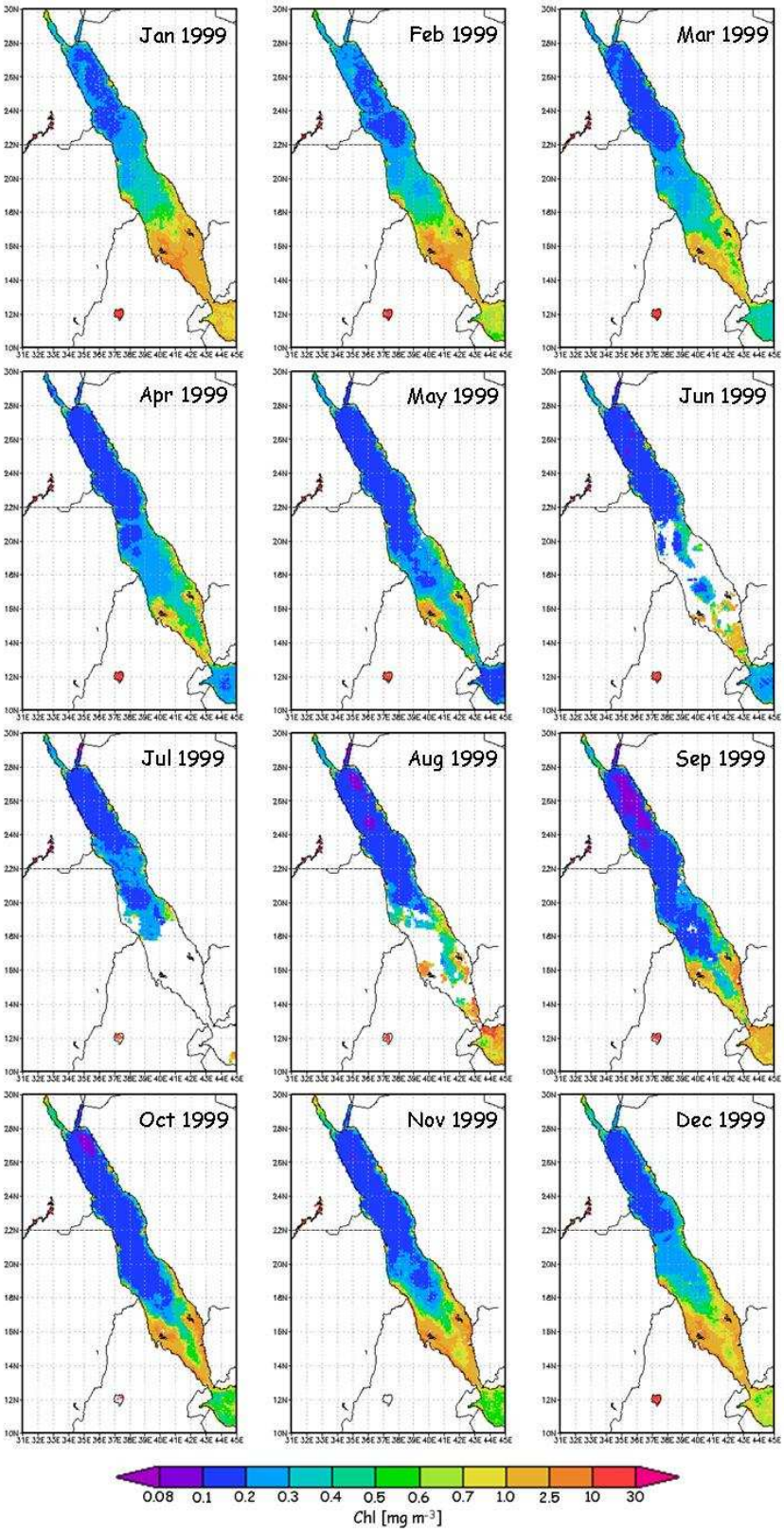

Plate 14. SeaWiFS-derived chl Monthly Means: 2000

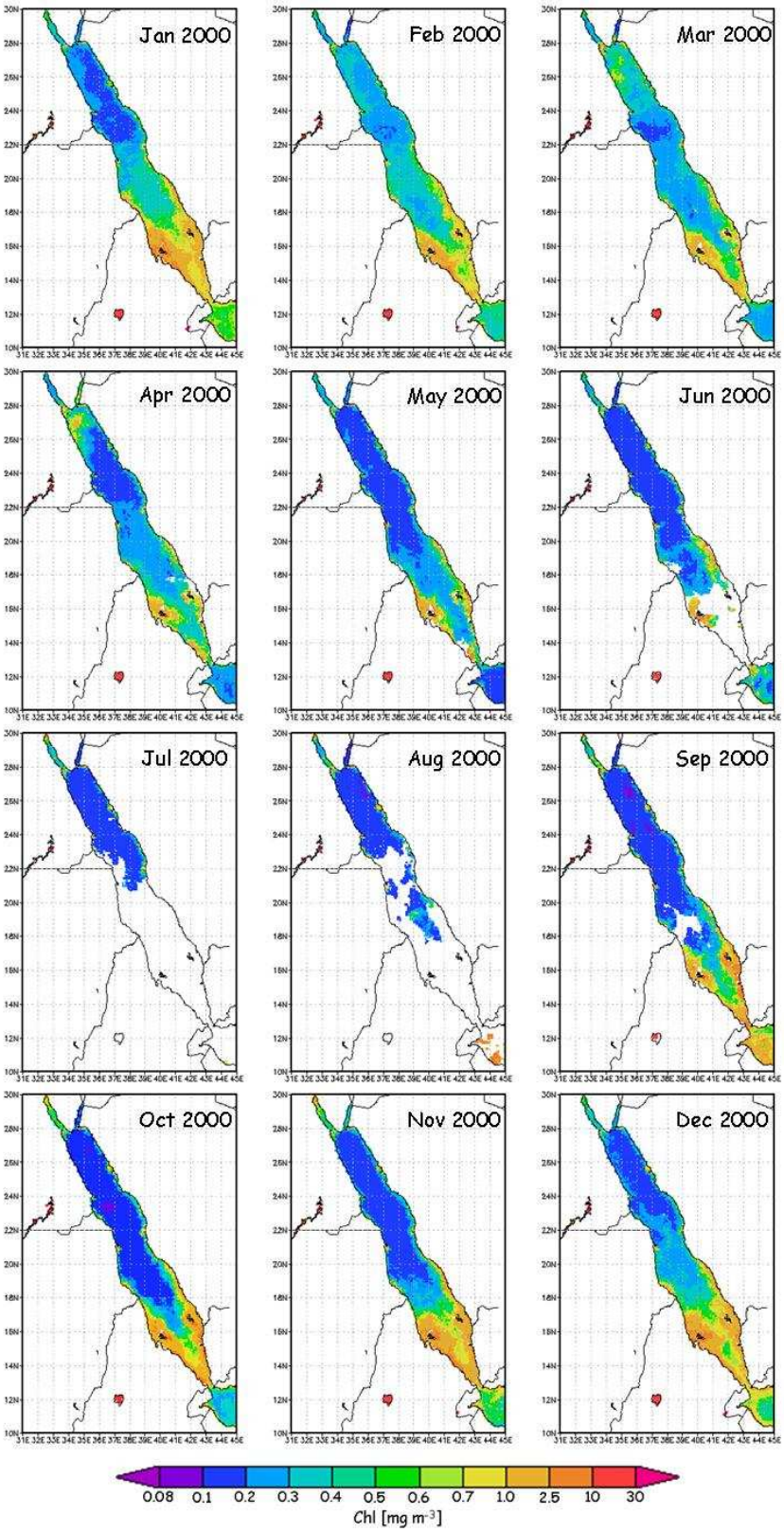

Plate 15. SeaWiFS-derived chl Monthly Means: 2001

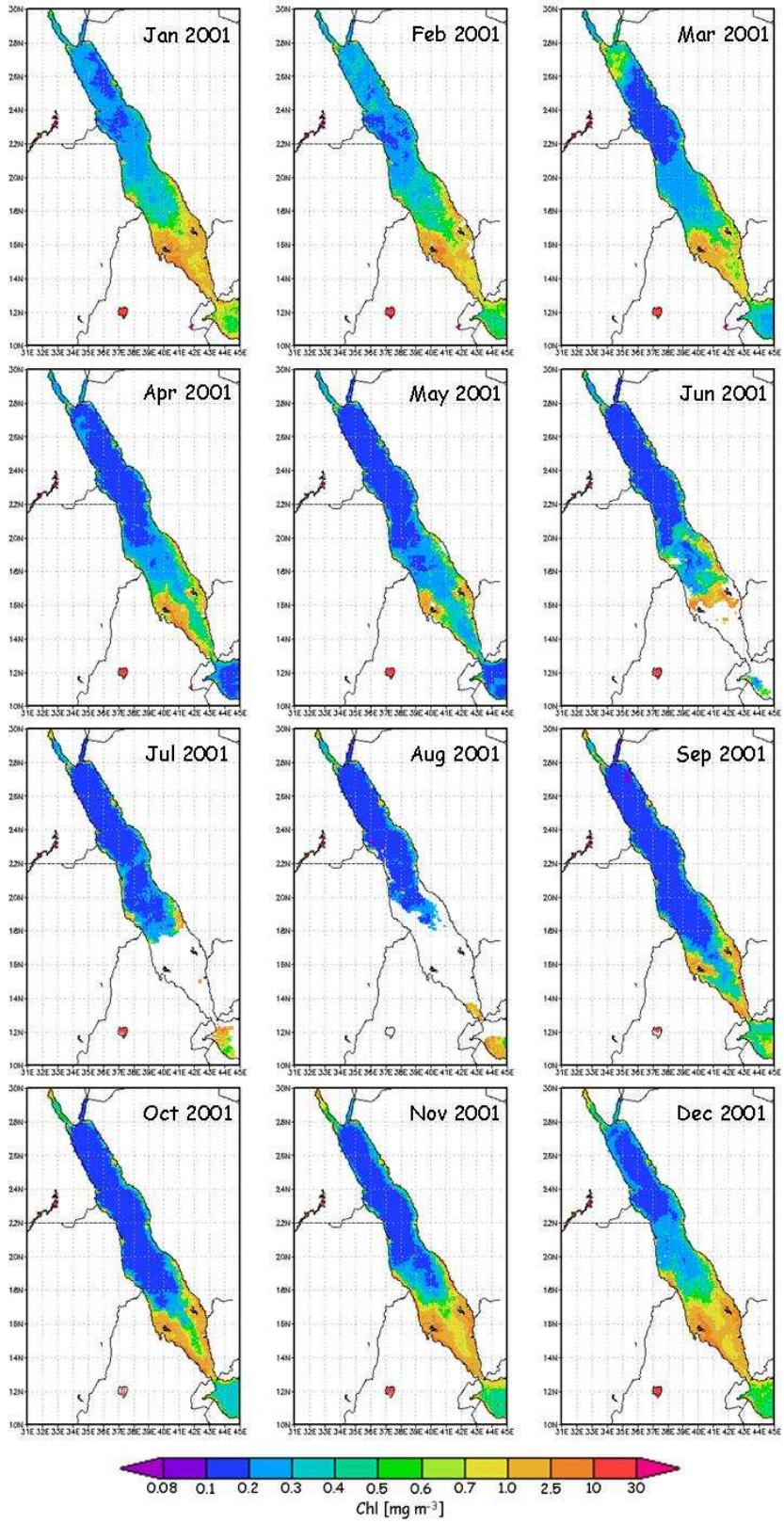

Plate 16. SeaWiFS-derived chl Monthly Means: 2002

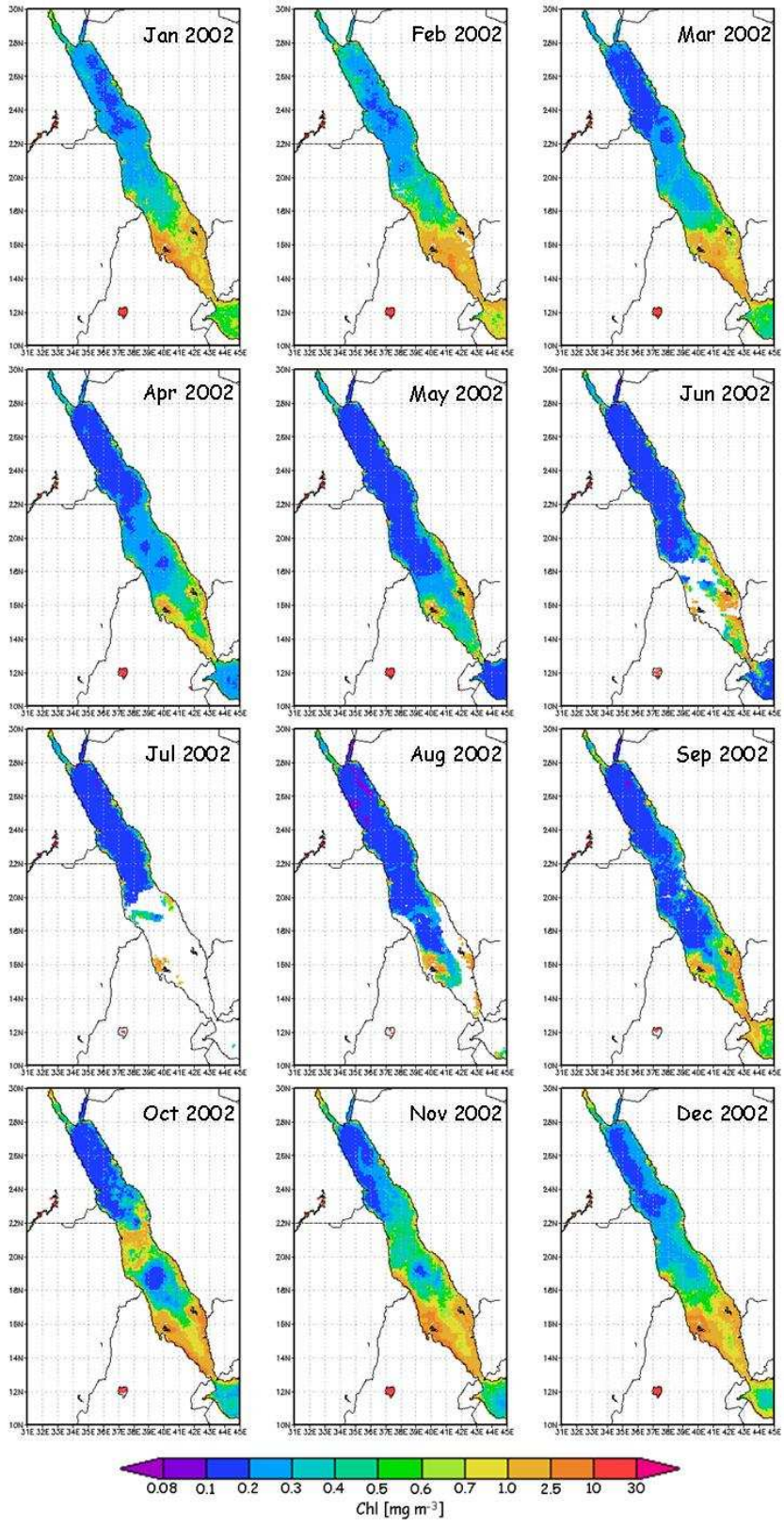

Plate 17. SeaWiFS-derived chl Monthly Means: 2003

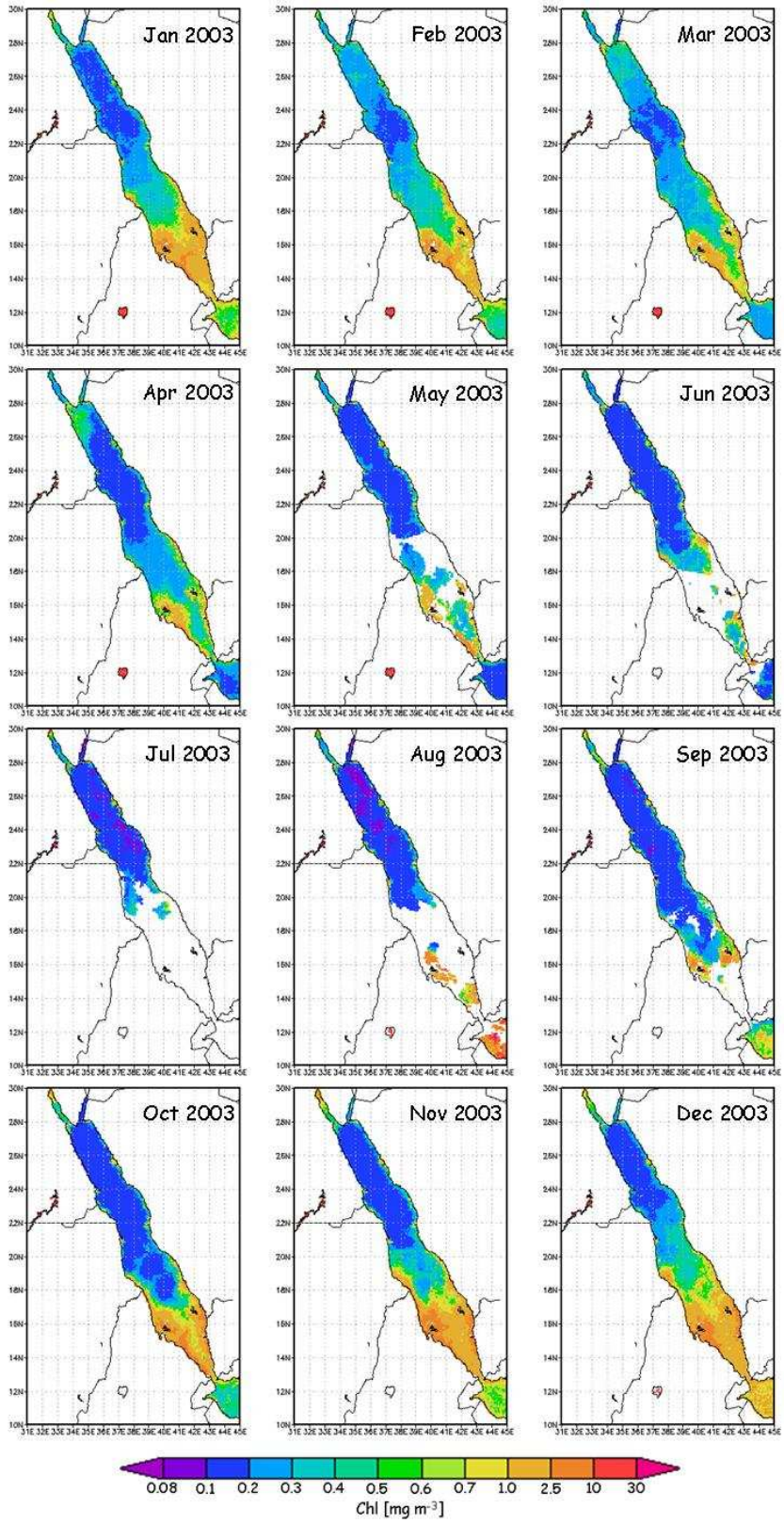

Plate 18. SeaWiFS-derived chl Monthly Means: 2004

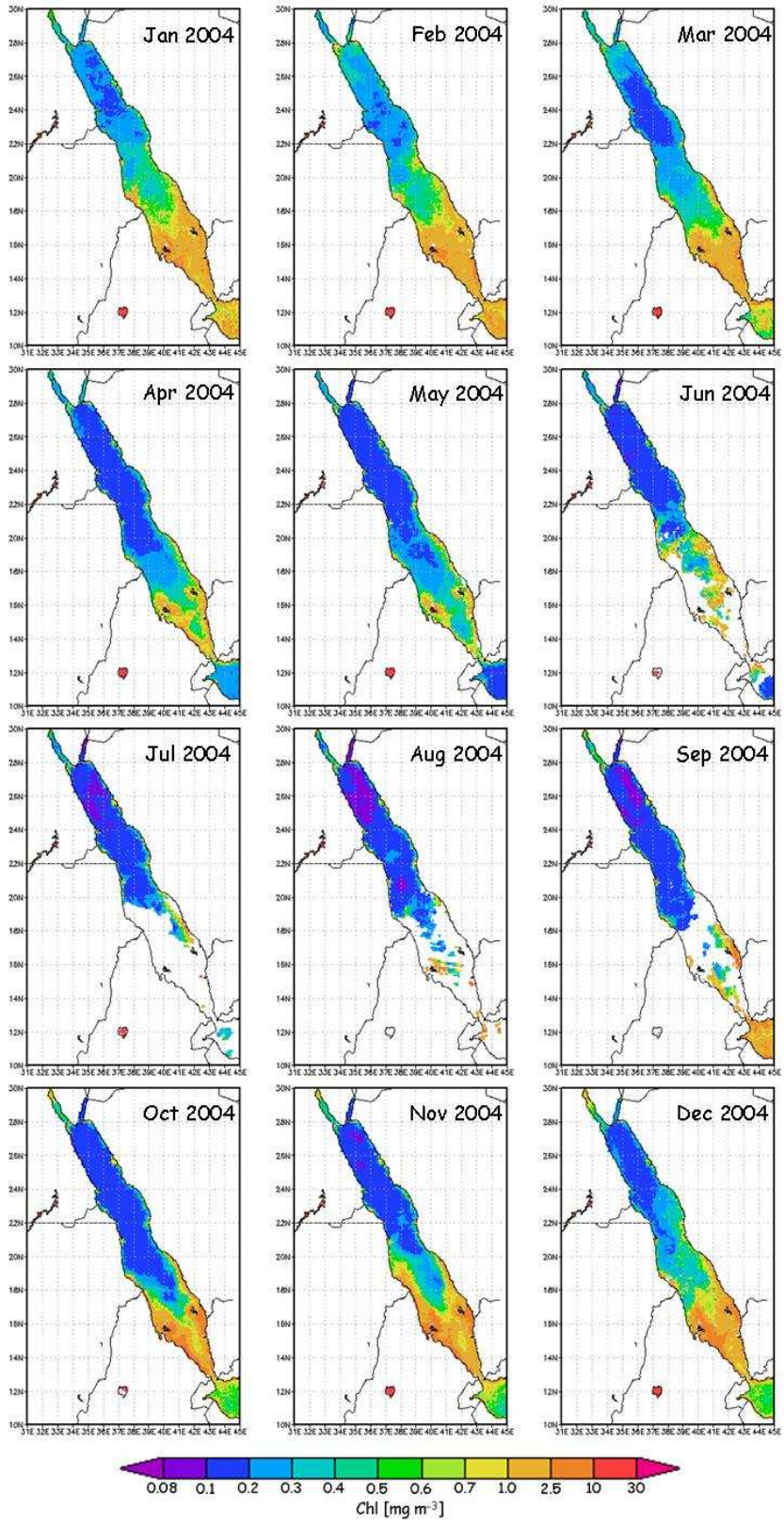

Plate 19. SeaWiFS-derived chl Monthly Means: 2005

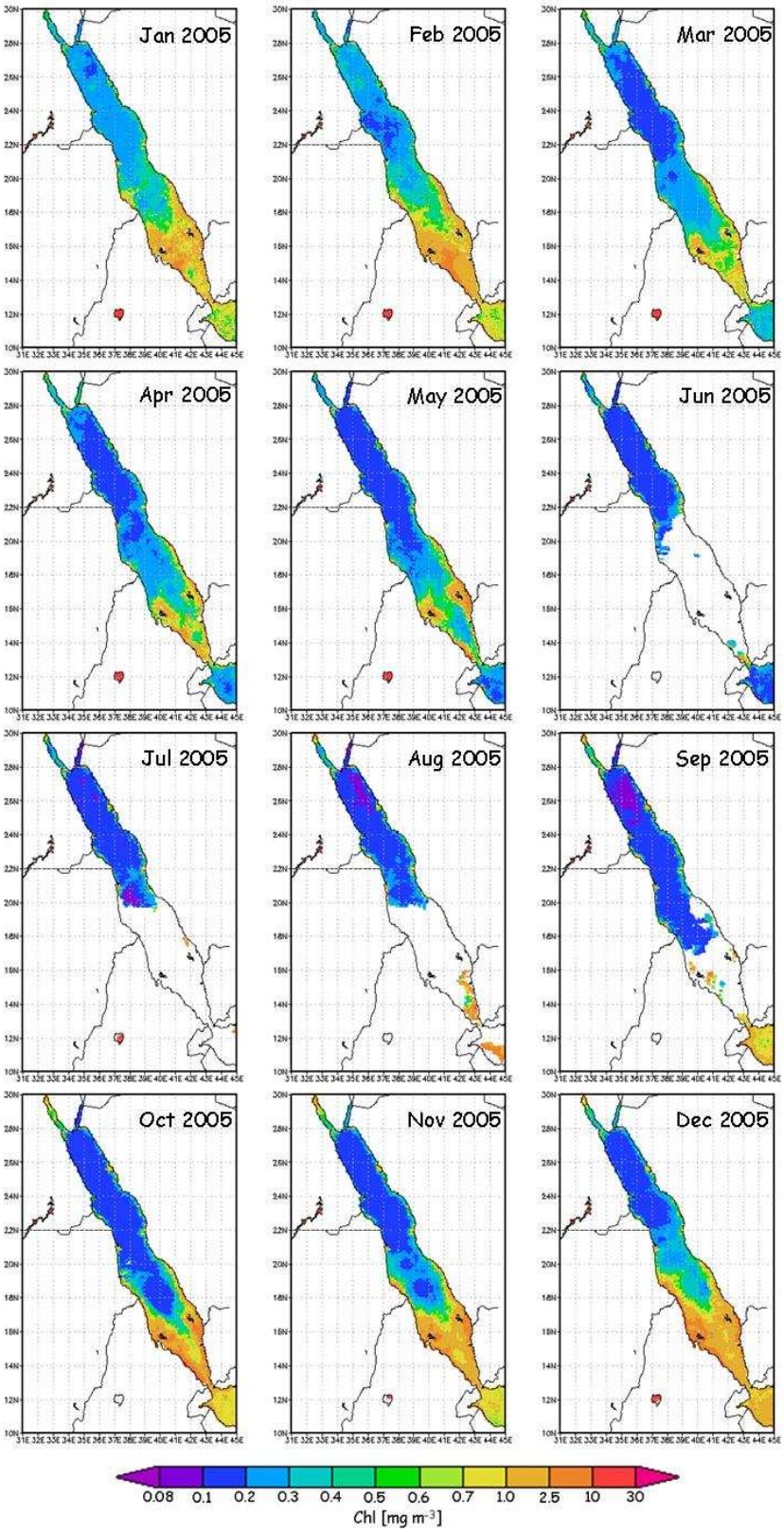

Plate 20. SeaWiFS-derived chl Monthly Means: 2006

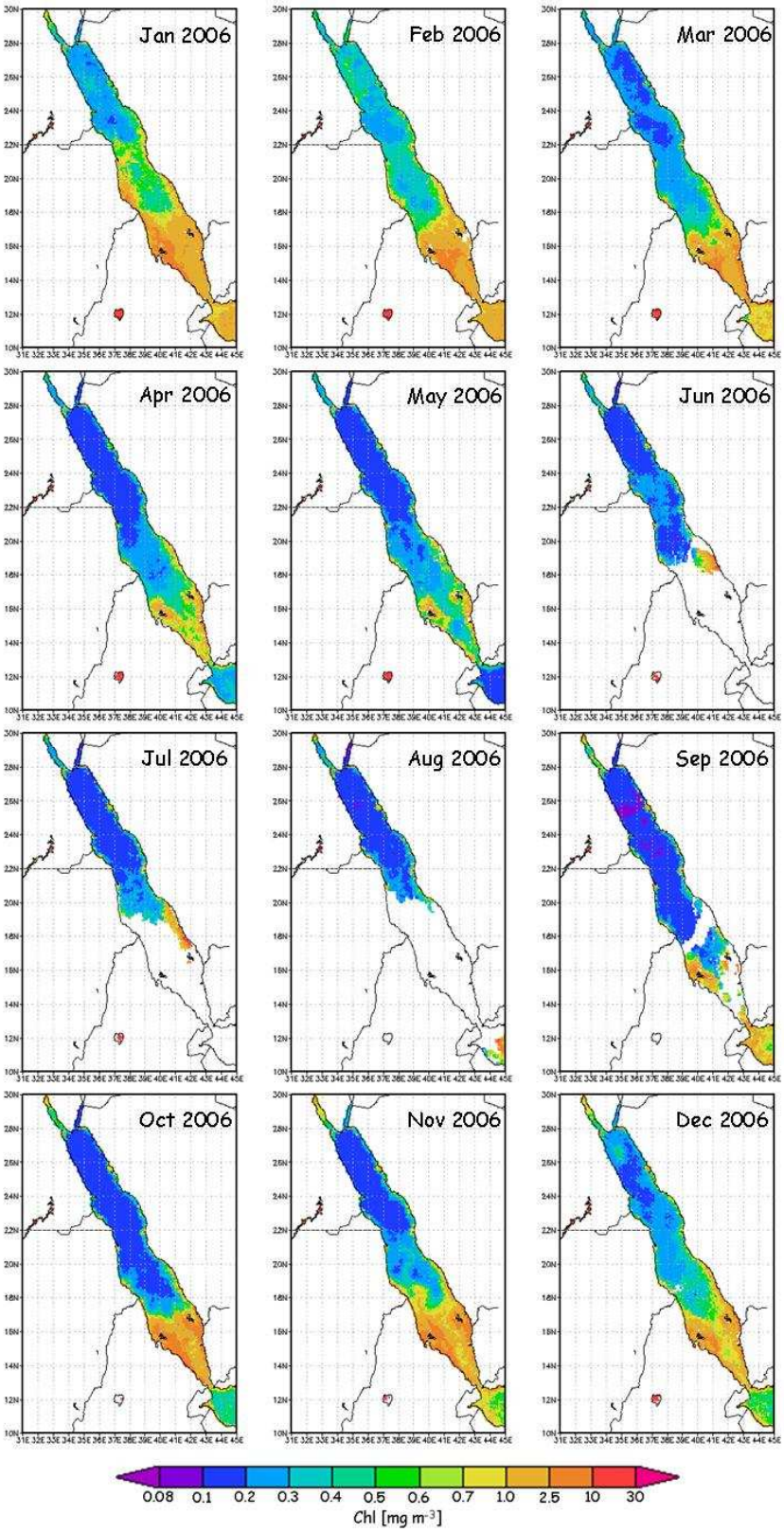

*Plate 21. Trend * of the chl Monthly Anomalies, ABV ***

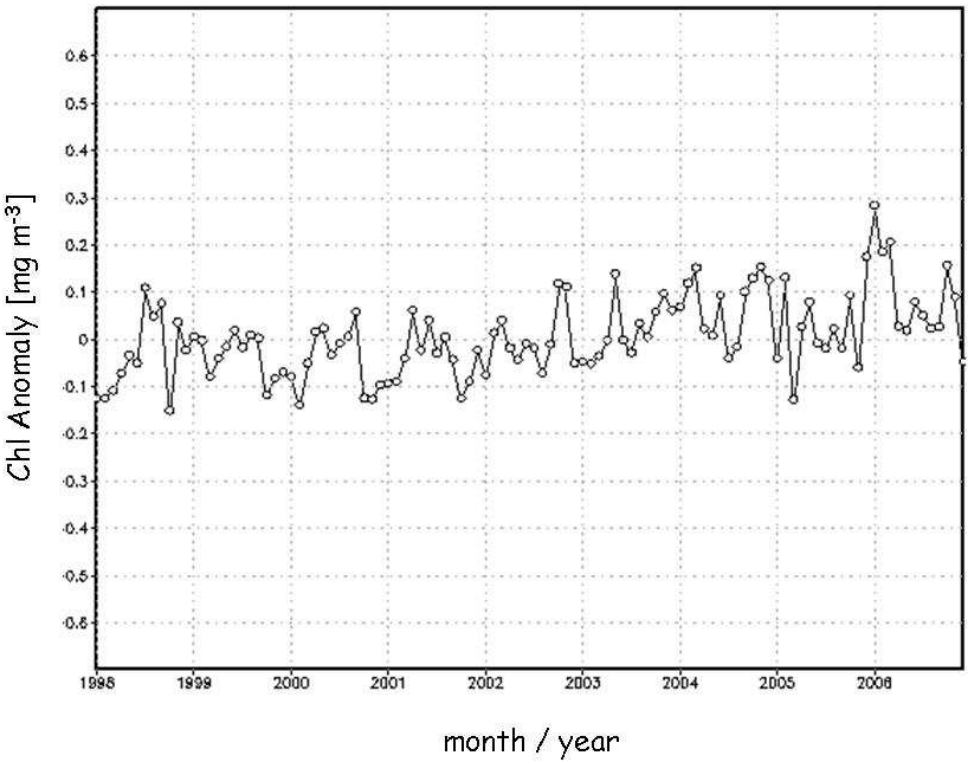

* Y axis: *chl* anomaly average basin value [mg m^{-3}], min – 0.7, max + 0.7, interval 0.1
X axis: months (January to December) and years (1998 to 2006)

** The Average Basin Value (ABV) is computed over the Red Sea area 12-28 N, 34-44 E; other regions considered to compute the *chl* climatological monthly mean trend are:
- the Northern Basin (22-28 N, 34-38 E),
- the Central Basin (18-22 N, 37-41 E),
- the Southern Basin (12-18 N, 38-44 E),
according to the following map subsets (shown on the *chl* climatological annual mean) :

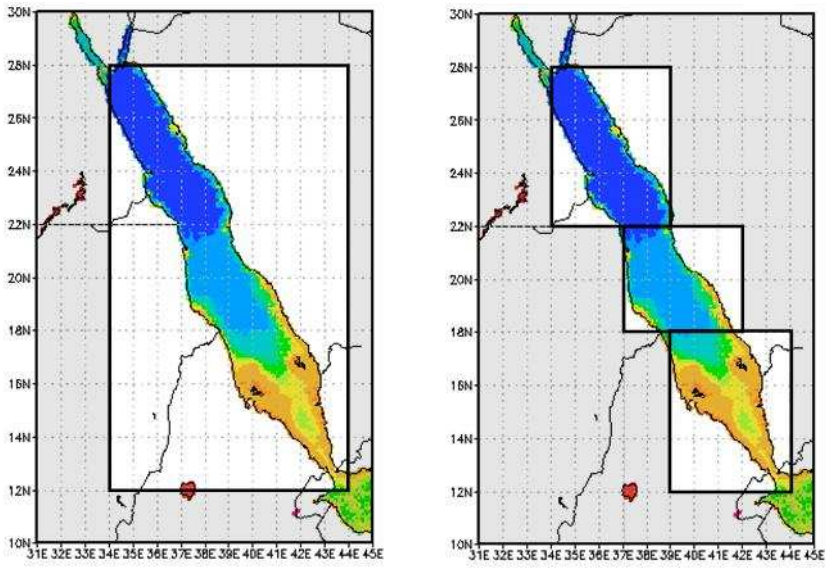

*Plate 22. Trend * of the chl Monthly Anomalies, sub-regions***

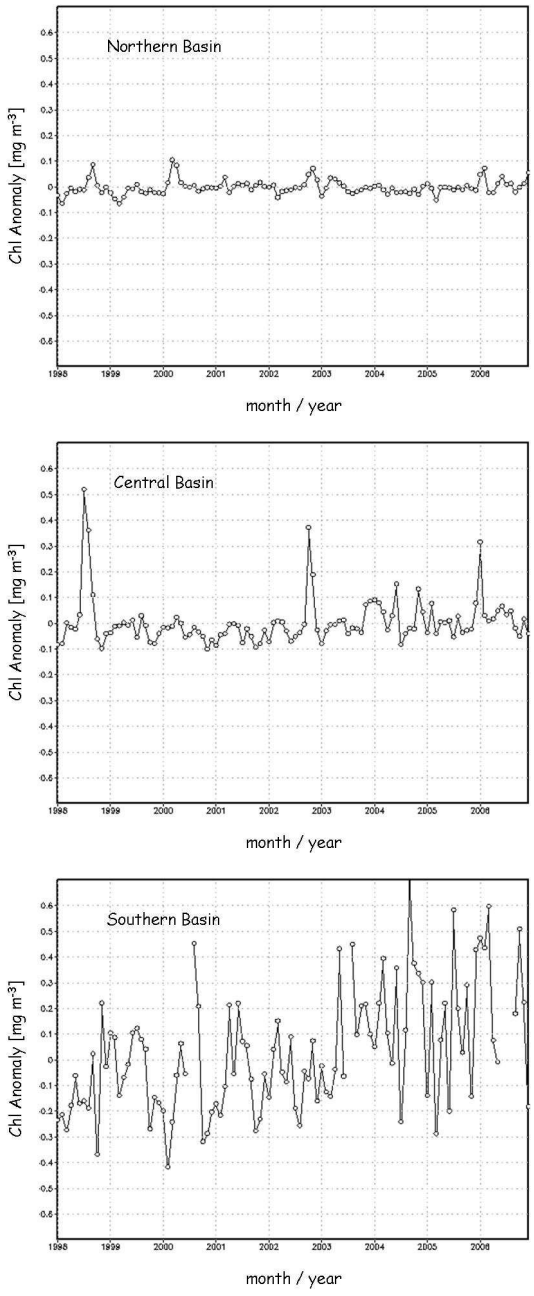

* Y axis: *chl* anomaly average basin value [mg m^{-3}], min – 0.7, max + 0.7, interval 0.1
X axis: months (January to December) and years (1998 to 2006)

** upper panel: Northern Basin (22-28 N, 34-38 E)
middle panel: Central Basin (18-22 N, 37-41 E)
lower panel: Southern Basin (12-18 N, 38-44 E)

4. Conclusion

Space and time heterogeneity of algal blooming in the Red Sea has been studied using a SeaWiFS-derived 9-year (1998-2006) time series of *chl* maps. Further, *chl* anomalies, computed with respect to the climatological maps of the same period, were also considered, to assess the degree of interannual variability. The imagery details the diverse characteristics of the northern (oligotrophic) sub-basin and the southern (mesotrophic)sub-basin, between which a central, transitional sub-basin presents more variable environmental conditions. Interestingly, hardly any subdivision between a strictly pelagic region and a costal zone appears anywhere in the Red Sea, with the exception of that occurring between the basin interior and the broad shelf areas, dotted by numerous islands, of the south.

The observed seasonal pattern is essentially bimodal, with a *fall-winter* period of extended blooming, which progresses from south to north, followed by a *spring-summer* period of less intense blooming episodes, occurring in both the central sub-basin and the southern sub-basin. Overall, the annual bio-geo-chemical cycle seems to be governed by the climatic characteristics of the basin, the monsoon regime in particular, and by the ensuing thermohaline circulation.

Given that fertilization in the Red Sea occurs mainly *via* the inflow from the Gulf of Aden and the southern part of the basin, *chl* values should indeed start to increase with the inflow of surface waters from the Gulf of Aden throughout phase one (October to December) of the *fall-winter* period. Thus, relative *chl* maxima appear first in the Southern Basin, between October and November, and then progress northward in the Central basin and Northern basin, between November and December. From December to January, Ekman transport due to the north-east monsoon would contribute to spread surface waters toward the northern region, thus fostering the *chl* absolute maximum observed during phase two (January to March) of the *fall-winter* period in the Northern Basin. The flux of nutrients of southern origin would then stop, or be much reduced, during the spring inter-monsoon, from March to May. Hence the decreasing *chl* values toward the end of the *fall-winter* period, and the continuing decrease in phase one (April to June) of the *spring-summer* period.

Following the May absolute minimum, starting in June and through phase two (July to September) of the *spring-summer* period, the intrusion of intermediate waters from the Gulf of Aden, driven by the south-west monsoon, would favour the mixing of deep nutrients into the upper layer of the Southern Basin. This could fertilize the Southern Basin and result in the *chl* relative maxima recurring in summer months, between July and September. At the end of this phase, following the September minimum, the conventional anti-estuarine regime of the Red Sea would take over again, with the Red

Sea overflow coupled to the inflow from the Gulf of Aden leading once again to the *fall-winter* situation detailed above.

The *chl* interannual variability of is not very pronounced, but there are hints of a steady *fall-winter* maxima increase, for most of the data set considered. The *chl* anomalies show limited oscillations around zero over the greater part of the basin. In the south, however, negative anomalies characterize the first half of the period considered, while positive anomalies prevail in the second half. A series of odd episodes are also highlighted by both anomaly record and trend of the *chl* large-scale average. Three of these episodes deserve further investigation.

The first anomalous episode (see Plate 23) is a massive bloom, possibly linked to an anticyclonic eddy, which occurred between the Northern Basin and the Central Basin during the late 1998 *spring-summer* period. An eddy-like structure, with a low *chl* core (compatible with downwelling associated to the convergence within an anticyclonic gyre), first appeared in the area between Port Sudan and Jeddah in June. The structure evolved into a ring of very high *chl* values in July, and then moved slightly northward, developing once again a large low *chl* core in August. By SSeptember, the ring turned into a sizeable patch of high *chl* values, which virtually disappeared in October.

The second anomalous episode (see Plate 24) concerns a low *chl* area, which developed between the Central Basin and the Southern Basin, from *spring-summer* to *fall-winter* of 2002. Traces of an eddy-like structure, with a low *chl* core, first appeared in the area north of the Dahlak Archipelago and Farasan Islands in August. The structure almost disappeared in September, but then materialized again in October, between massive blooms in the Central Basin and Southern Basin. As the bloom in the Central Basin decayed, in November and December, the patch started to reduce in size and almost disappeared. However, a meandering structure of higher *chl* values, which possibly had curled upon itself to isolate the low *chl* patch in the basin interior, continued to be present along the eastern side of the entire basin.

The third anomalous episode (see Plate 25) is again a sizeable bloom, possibly linked to a series of anticyclonic eddies, which occurred in the Central Basin, during the 2005-2006 *fall-winter* period. A first eddy-like structure, with a low *chl* core, appeared in the area off (and south of) Port Sudan in October 2005. This evolved into two smaller eddy-like structures, again with low *chl* cores, in November 2005. By December 2005, the eddies had disappeared, only to be replaced by a patchy bloom occupying all of the Southern Basin and, with somewhat reduced intensity, the Central Basin as well. The bloom continued, augmented and extended to the entire basin, in January 2006 and chiefly in February 2006. Only in March 2006 the *chl* levels started to decrease again to more seasonable values.

Plate 23. Anomalous features, 1998 chl Monthly Means

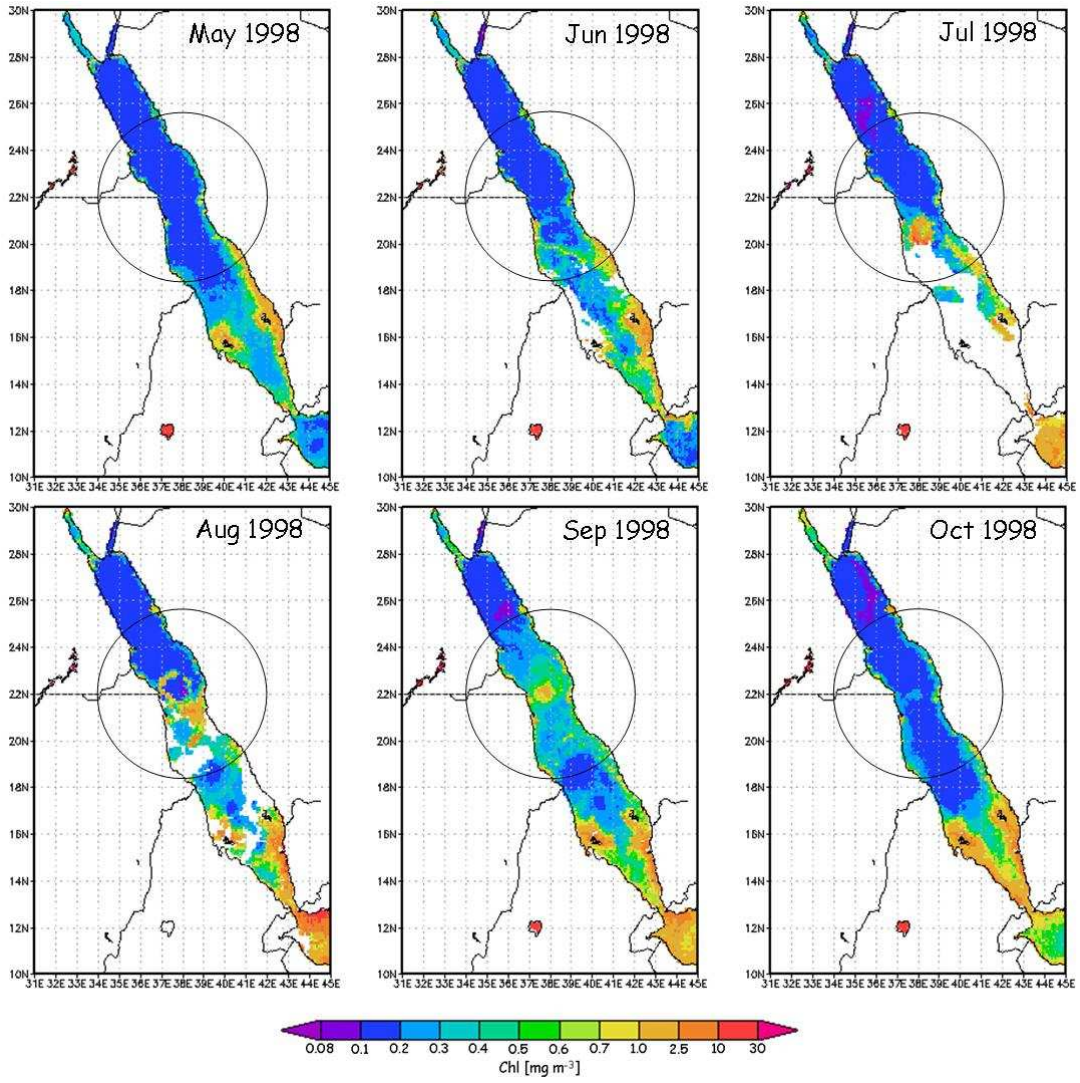

Plate 24. Anomalous features, 2002 chl Monthly Means

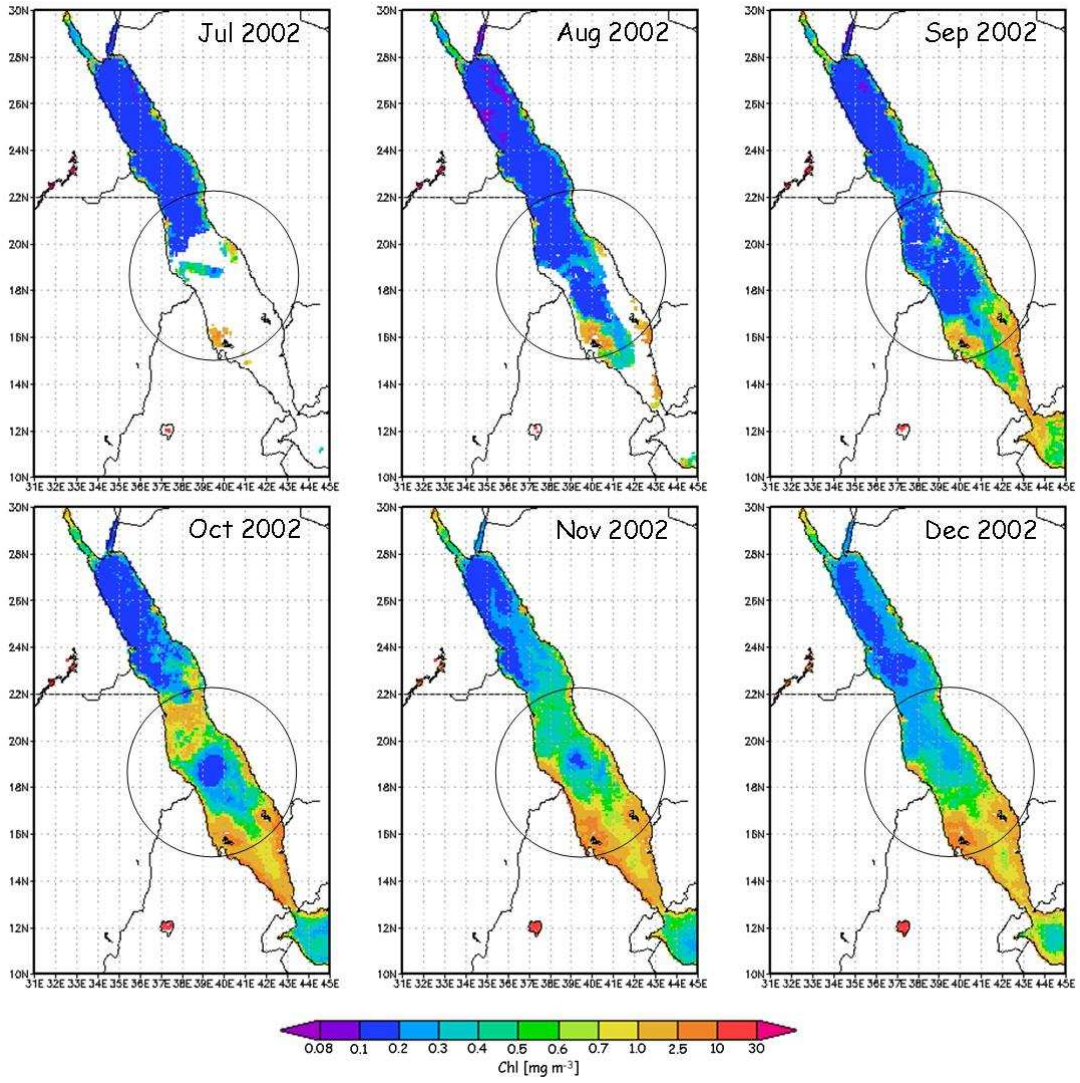

Plate 25. Anomalous features, 2005-2006 chl Monthly Means

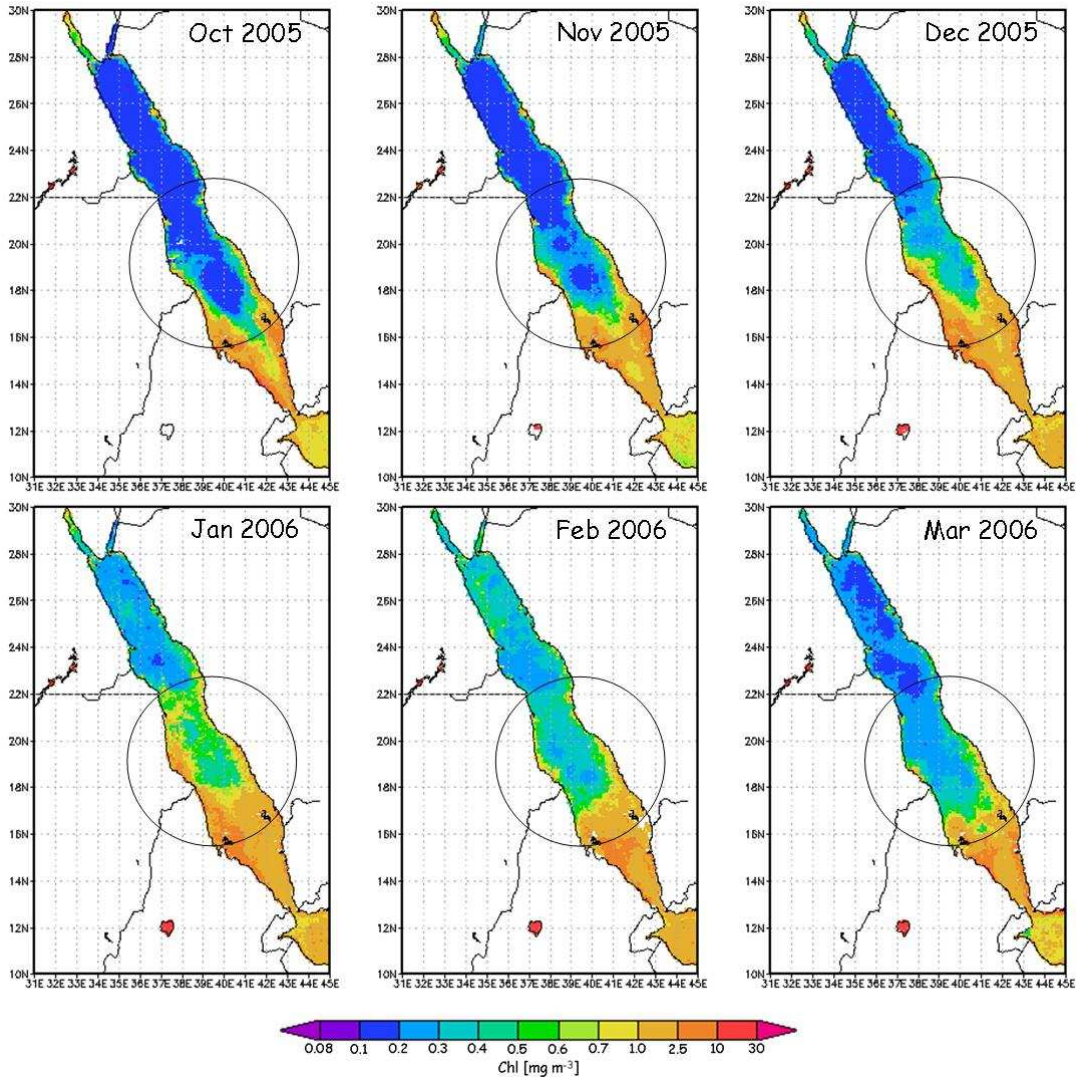

References

Baith, K., R. Lindsay, G. Fu, and C.R. McClain (2001). "SeaDAS, a data analysis system for ocean-color satellite sensors". *EOS Transactions AGU*, 82. p. 202.

Barale, V. (1994). "Ocean colour, planktonic pigments & productivity". *Memoires de l'Institut Oceanographique, Monaco*, n. 18, p. 23-33.

Barale, V., J.M. Jaquet, K. Allenbach, M. Ndiaye, and A. Hoareau (2005). B*io-optical Environmental Assessments of Marginal Seas. Progress Report 2.* European Commission, EUR 21899 EN, pp. 63.

Barale, V., and J.M. Jaquet (2006). *Bio-optical Environmental Assessments of Marginal Seas. Progress Report 3*. European Commission, EUR 22479 EN, pp. 62.

Barale, V., B. Weber, and J.M. Jaquet (2004). *Bio-optical Environmental Assessments of Marginal Seas. Progress Report 1*. European Commission, EUR 21479 EN, pp. 50.

Bower, A.S., H.D. Hunt, and J.F. Price (2000). Character and dynamics of the Red Sea and Persian Gulf outflows. *Journal of Geophysical Research*, vol. 105, p. 6387-6414.

Campbell, J.W., J.M. Blaisdell, and M. Darzi (1995). "*Level-3 SeaWiFS Data Products: Spatial and Temporal Binning Algorithms*". SeaWiFS Technical Report Series, Volume 32, NASA Technical Acker, Eds., NASA Goddard Space Flight Center, Greenbelt, MD.

Edwards, A.J. (1987). Climate and Oceanography. In: A.J. Edwards and S.M. Head ed.s, *Red Sea: Key Environments*, Pergamon Press, Oxford, p. 45-69.

Eschel, G., M.A. Cane, and M.B. Blumenthal (1994). Modes of subsurface, intermediate, and deep water renewal in the Red Sea. *Journal of Geophysical Research*, vol. 99, p. 15941-15952.

Gladstone, W., N. Tawfiq, D. Nasr, I. Andersen, C. Cheung, H. Drammeh, F. Krupp, and S. Lintner (1999). Sustainable use of renewable resources and conservation in the Red Sea and Gulf of Aden: issues, needs and strategic actions. *Ocean and Coastal Management*, vol. 42, p. 671-697.

Grassen, G., and D. Kroon (1991). Evidence for Red Sea surface circulation from oxygen isotopes of modern surface waters and planktonic foraminiferal test. *Paleoceanography*, vol. 6, p. 73-

82.

Gregg, W.W., and N.W. Casey (2004). Global and regional evaluation of the SeaWiFS chlorophyll data set. *Remote Sensing of Environment*, vol. 93 (4), p. 463-479.

Head, S.M. (1987). Red Sea fisheries. In: A.J. Edwards and S.M. Head ed.s, *Red Sea: Key Environments*, Pergamon Press, Oxford, p. 363-382.

International Hydrographic Organization (1953). *Limits of Oceans and Seas*. Special Publication No. 23, 3rd Edition, Imp. Monégasque, Monte Carlo, pp. 39.

McClain, C.R., G.C. Feldman, and S.B. Hooker (2004). "An overview of the SeaWiFS project and strategies for producing a climate research quality global ocean bio-optical time series". *Deep-Sea Research,* vol. II 51, p. 5-42.

Morcos, S.A. (1970). Physical and chemical oceanography of the Red Sea. *Oceanography Marine Biology Annual Review*, vol. 8, p. 73-202.

Murray, S.P., and W. Jones (1997). Direct observations of seasonal exchange through the Bab al Mandab Strait. *Geophysical Research Letters*, vol. 24, p. 2557-2560.

PERSGA (1998). Strategic Action Program for the Red Sea and Gulf of Aden. PERSGA, Jeddah, p. 69.

Quadfasel, D., and H. Baudner (1993). Gyre-scale circulation cells in the Red Sea. *Oceanologica Acta*, vol. 16, p. 221-229.

Sheppard, C., A. Prince, and C. Roberts (1992). Marine Ecology of the Arabian Region. Academic Press, London.

Sheppard, C.R.C. (2000). The Red Sea. In: C.R.C. Sheppard ed., *Seas at the Millennium: and Environmental Evaluation*, Pergamon Press, Oxford, p. 35-45.

Siedler, G. (1969). General circulation of the water masses in the Red Sea. In: E.T. Degens and D.A. Ross ed.s, *Hot Brines and Recent Heavy Metals Deposits in the Red Sea*, Springer-Verlag, Berlin, p. 131-137.

Smeed, D.A. (1997). Seasonal variations of the flow in the strait of Bab el Mandab. *Oceanologica Acta*, vol. 20, p. 773-781.

Smeed, D.A. (2000). Hydraulic control of three-layer exchange flows: application to the Bab el Mandab. *Journal of Physical Oceanography*, vol. 30, p. 2574-2588.

Sofianos, S., W.E. Johns, and S.P. Murray (2002). Heat and freshwater budgets in the Red Sea from direct observations at Bab el Mandab. *Deep-Sea Research*, vol. II 49, p. 1323-1340.

Tesfamichael, D., and T.J. Pitcher (2006). Multidisciplinary evaluation of the sustainability of Red Sea Fisheries using Rapfish. *Fisheries Research*, vol. 78 (2-3), p. 227-235.

European Commission

EUR 23091 EN – Joint Research Centre – Institute for Environment and Sustainability
Title: Marine and Coastal features of the Red Sea
Author: V. Barale
Luxembourg: Office for Official Publications of the European Communities
2007 – 56 pp. – 21.0 x 29.7 cm
EUR – Scientific and Technical Research series – ISSN 1018-5593

Abstract
Patterns of algal blooming, described by variations in the abundance of planktonic agents, are considered to be indicators of the ecological balance in coastal and marine environments. A time series of *chl* statistical maps and anomalies, derived from data collected by the Sea-viewing Wide Field-of-View Sensor (SeaWiFS), from January 1998 to December 2006, were considered to explore the space and time heterogeneity of algal blooming in the Red Sea. The imagery details the diverse characteristics of the northern (oligotrophic) sub-basin and the southern (mesotrophic) sub-basin, between which a central, transitional sub-basin presents more variable environmental conditions. The observed seasonal pattern is essentially bimodal, with a *fall-winter* period of extended blooming, followed by a *spring-summer* period of less intense blooming episodes, occurring in both the central sub-basin and the southern sub-basin. Overall, the annual bio-geo-chemical cycle seems to be governed by the climatic characteristics of the basin, the monsoon regime in particular, and by the ensuing thermohaline circulation. The *chl* interannual variability is not very pronounced, but there are hints of a steady *fall-winter* maxima increase, for most of the data set considered. The *chl* anomalies show limited oscillations around zero over the greater part of the basin. In the south, however, negative anomalies characterize the first half of the period considered, while positive anomalies prevail in the second half. A series of odd blooming episodes are also highlighted by both anomaly record and trend of the *chl* large-scale average.

How to obtain EU publications

Our priced publications are available from EU Bookshop (http://bookshop.europa.eu), where you can place an order with the sales agent of your choice.

The Publications Office has a worldwide network of sales agents. You can obtain their contact details by sending a fax to (352) 29 29-42758.

The mission of the JRC is to provide customer-driven scientific and technical support for the conception, development, implementation and monitoring of EU policies. As a service of the European Commission, the JRC functions as a reference centre of science and technology for the Union. Close to the policy-making process, it serves the common interest of the Member States, while being independent of special interests, whether private or national.